arXiv:2407.17420v2 [q-bio.CB] 26 Jul 2024

Cell shape and orientation control galvanotactic accuracy

Ifunanya Nwogbaga[1] and Brian A. Camley[1,2]
[1]*Department of Biophysics, Johns Hopkins University, Baltimore, MD 21218*
[2]*Department of Physics & Astronomy, Johns Hopkins University, Baltimore, MD 21218*

Eukaryotic cells sense and follow electric fields during wound healing and embryogenesis – this is called galvanotaxis. Galvanotaxis is believed to be driven by the redistribution of transmembrane proteins and other molecules, referred to as "sensors", through electrophoresis and electroosmosis. Here, we update our previous model of the limits of galvanotaxis due to stochasticity of sensor movements to account for cell shape and orientation. Computing the Fisher information, we find that cells in principle possess more information about the electric field direction when their long axis is parallel to the field, but that for weak fields maximum-likelihood estimators of the field direction may actually have lower variability when the cell's long axis is perpendicular to the field. In an alternate possibility, we find that if cells instead estimate the field direction by taking the average of all the sensor locations as its directional cue ("vector sum"), this introduces a bias towards the short axis, an effect not present for isotropic cells. We also explore the possibility that cell elongation arises downstream of sensor redistribution. We argue that if sensors migrate to the cell's rear, the cell will expand perpendicular the field – as is more commonly observed – but if sensors migrate to the front, the cell will elongate parallel to the field.

INTRODUCTION

Electric fields play a pivotal role in biological systems. The pioneering experiments of Luigi Galvani in the 18th century on muscle contractions in frog legs [1–3] are some of the earliest examples showcasing their significance. Direct current (DC) electric fields with strengths ranging from 30–100 mV/mm have been measured within and around developing embryos [4, 5], though applying additional electric fields to embryos cause abberations in embryonic development [6, 7]. Endogenous electric fields in the range of 40–200 mV/mm also emerge around wounds [8–11]. Applying additional electric fields during wound healing accelerates the healing process [12–15]. These electric fields have been shown to stimulate various types of cells to undergo galvanotaxis (alternately "electrotaxis"), a phenomenon where cells migrate directionally in response to the electric field. Examples of galvanotaxing cells include keratocytes [16–18], keratinocytes [8, 19, 20], granulocytes [21–23], fibroblasts [24–26], and neural crest cells [22, 27, 28]. Some cells such as keratocytes and neural crest cells respond to field strengths as low as 25 mV/mm [16] and 10 mV/mm [22], respectively.

There exists a consensus that cells sense electric fields through transmembrane molecule redistribution, which occurs via electrophoresis and electroosmosis. Simply put, proteins and other molecules on the cell surface are pulled by the electric field and migrate relative to the field, accumulating on one side of the cell. This redistribution of membrane-bound components is crucial for the initiation of galvanotaxis [16, 17, 26, 29–31]. Putative sensor candidates identified or hypothesized in the past include EGFR, P_2Y , integrins, and lipid rafts [32–36]. Different cell types, of course, may have different sensors, and there may be more than one sensor. Ion channels have also been observed to play a role [20, 37], suggesting there may be multiple mechanisms for sensing the field orientation [38].

In our previous manuscript [30], we determined the physical limits of galvanotactic measurement through sensor redistribution for round cells (circular and spherical). We developed a model that quantified how cells measure the direction of the electric field by using maximum likelihood estimation (MLE). In our approach, we assume that cells sense electric fields solely through redistribution of their transmembrane sensors. We discovered that circular cells can predict the field's direction efficiently by employing a simple strategy: the cell follows the direction of the average position of the sensors on its surface. We call this strategy "vector sum". The same result holds in 3D for spherical cells. This result comes naturally out of MLE – for round cells, MLE and vector sum produce the same measurement, though we find in this work this is not always true. In this manuscript, we extend the work of [30] to investigate how the shape and orientation of an elliptical cell influence its estimate of the field direction.

We want to find the factors limiting the accuracy of a cell's estimate $\hat{\psi}$ of the angle of the applied field ψ. To do this, we calculate the electric field around the cell, which controls the velocity of the sensors. We use this field to find the concentration of sensors around the cell arising from the competition between diffusion and electromigration. We construct a probability distribution of the sensor location from the concentration, and use maximum likelihood and an extended Cramér-Rao bound to quantify the cell's estimate of the electric field direction and its variance [30]. Surprisingly, whether the cell is more accurate in sensing the field's orientation when its long axis is parallel to or perpendicular to the field direction depends on the strength of the field and the method the cell uses to interpret the sensor location. Under the most likely experimental conditions, cells are better sensors of field orientation when the field is perpendicular to the

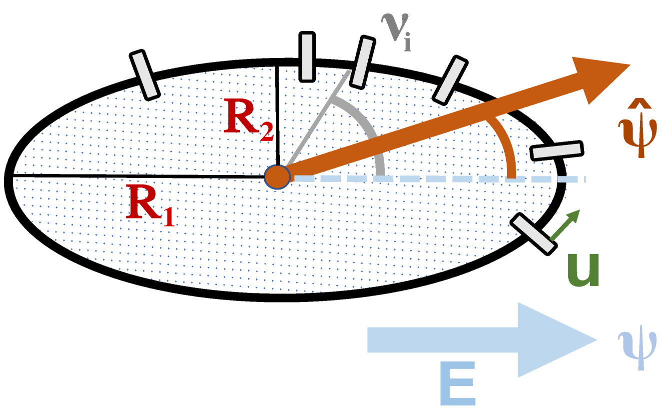

FIG. 1: Illustration of sensors on the surface of an elliptical cell; sensors are labeled by their elliptic angle location ν_i and traveling with velocity u. The cell is in an electric field pointing along the angle ψ and measures an estimated angle $\hat{\psi}$.

cell's long axis, as in chemotaxis [39]. However, the difference in accuracy between the best and worst orientations may not be large if the cell uses a maximum-likelihood estimate of the field. If the cell instead uses a simpler-to-compute "vector sum" estimate, its estimate will be biased, but can in some circumstances be quite close to the maximum-likelihood estimate, while at stronger fields, the cell can be quite far from the best possible estimate, and its accuracy will depend much more strongly on cell orientation relative to the field. We also address the possibility that the cell can change shape in response to an applied field, hypothesizing that cells extend radially proportional the level of sensor concentration in a graded radial extension-style model [40–42]. We find this predicts that the cell would lengthen along the field direction if the sensors are at the front of the cell, contrary to known observations [43], but lengthen perpendicular to the field if the sensors are at the back of the cell. These results suggest a potential way to determine the sign of the sensor mobility – something our earlier work did not constrain.

MODEL AND METHODS

We describe our cell as a two-dimensional ellipse, characterized by major and minor axes R_1 and R_2. $\lambda = R_1/R_2$ is the cell's aspect ratio. Throughout this paper, we will choose coordinates so that the cell is elongated along the x-direction – the field direction may vary but the cell's long axis direction is always consistent. Motivated by [16, 30, 31], we claim that the cell senses the electric field direction ψ via electromobile sensors (Fig. 1), producing an estimate of the field direction $\hat{\psi}$. Given the geometry, we use elliptic coordinates (μ, ν), where μ is the elliptic radius and ν is the elliptic angle, with corresponding unit vectors $\hat{\boldsymbol{\mu}}(\mu,\nu)$ and $\hat{\boldsymbol{\nu}}(\mu,\nu)$ (see Appendix A). $\hat{\boldsymbol{\mu}}$ is normal to the cell surface while $\hat{\boldsymbol{\nu}}$ is tangential to the surface.

Calculation of the external electric field

The motion of sensors on the cell boundary is dependent on the local electric field [17, 29, 30]. To find the electric field at the boundary of the cell, we solve Laplace's equation $\nabla^2\Phi = 0$ for the electric potential Φ in elliptic coordinates, subject to the conditions that far away from the cell $\Phi = -E_0(x\cos\psi + y\sin\psi)$, and at the cell boundary the gradient of the potential vanishes normal to the cell surface, i.e. the electric field is solely tangential to the membrane. The latter condition is valid for a nonconductive membrane [44, 45]. This assumption is appropriate since the resistivity of the membrane is much higher than that of the solution and cytoplasm (see Appendix B). Subsequently, the electric field around the cell is solely determined by the cell shape [44, 45] (Fig. 2). The solution to Laplace's equation in elliptic coordinates is well known [46, 47]. When an external field $\mathbf{E}_{\text{ext}} = E_0(\cos\psi, \sin\psi)$ is applied to the cell, the electric field outside the cell is

$$\begin{aligned}\mathbf{E} = {} & \frac{E_0 a}{h_\mu}\frac{e^{\mu} - e^{2\mu_0-\mu}}{2}\cos(\nu-\psi)\hat{\boldsymbol{\mu}} \\ & -\frac{E_0 a}{h_\mu}\frac{e^{\mu} + e^{2\mu_0-\mu}}{2}\sin(\nu-\psi)\hat{\boldsymbol{\nu}}.\end{aligned} \tag{1}$$

The cell has foci at $\pm a$, with $a = \sqrt{R_1 - R_2}$ (see Appendix A); the cell's boundary is at $\mu = \mu_0$. The scale factor $h_\mu(\mu,\nu) = a\sqrt{(\cosh 2\mu - \cos 2\nu)/2}$. This is the usual curvilinear scale factor for elliptic coordinates, $h_\mu = |\partial\mathbf{r}/\partial\mu|$. The field tangent to the cell at the boundary $\mu = \mu_0$ is proportional to the unit vector $\hat{\boldsymbol{\nu}}$, which points in the direction tangential to the cell surface

$$\mathbf{E}_{\parallel} = -E_0\frac{ae^{\mu_0}}{h_{\mu_0}}\sin(\nu-\psi)\hat{\boldsymbol{\nu}}, \tag{2}$$

where the scale factor $h_{\mu_0} \equiv h_\mu(\mu_0,\nu)$. Note that $ae^{\mu_0} = a\cosh\mu_0 + a\sinh\mu_0 = R_1 + R_2$. The largest magnitudes of $\mathbf{E}_{\parallel}$ are naturally where the applied field is parallel to the local surface of the cell. This means that when the applied field is parallel to the long axis of the cell ($\psi = 0$), the local tangential field $\mathbf{E}_{\parallel}$ is largest along the long side of the cell, tending to concentrate sensors to the narrow tips of the cell. By contrast, if the field is perpendicular to the cell, the tangential field is largest at the narrow tips of the cell, and the sensors are pulled toward the broad side of the cell, though they are not as strongly concentrated. Plots of $\mathbf{E}_{\parallel}$ are shown in Appendix D.

Transport of sensors along boundary and probability distribution

Armed with an expression for the electric field everywhere around the cell, we can now calculate the transport of sensors at the cell boundary. The sensors move following the tangential field to the surface, traveling along

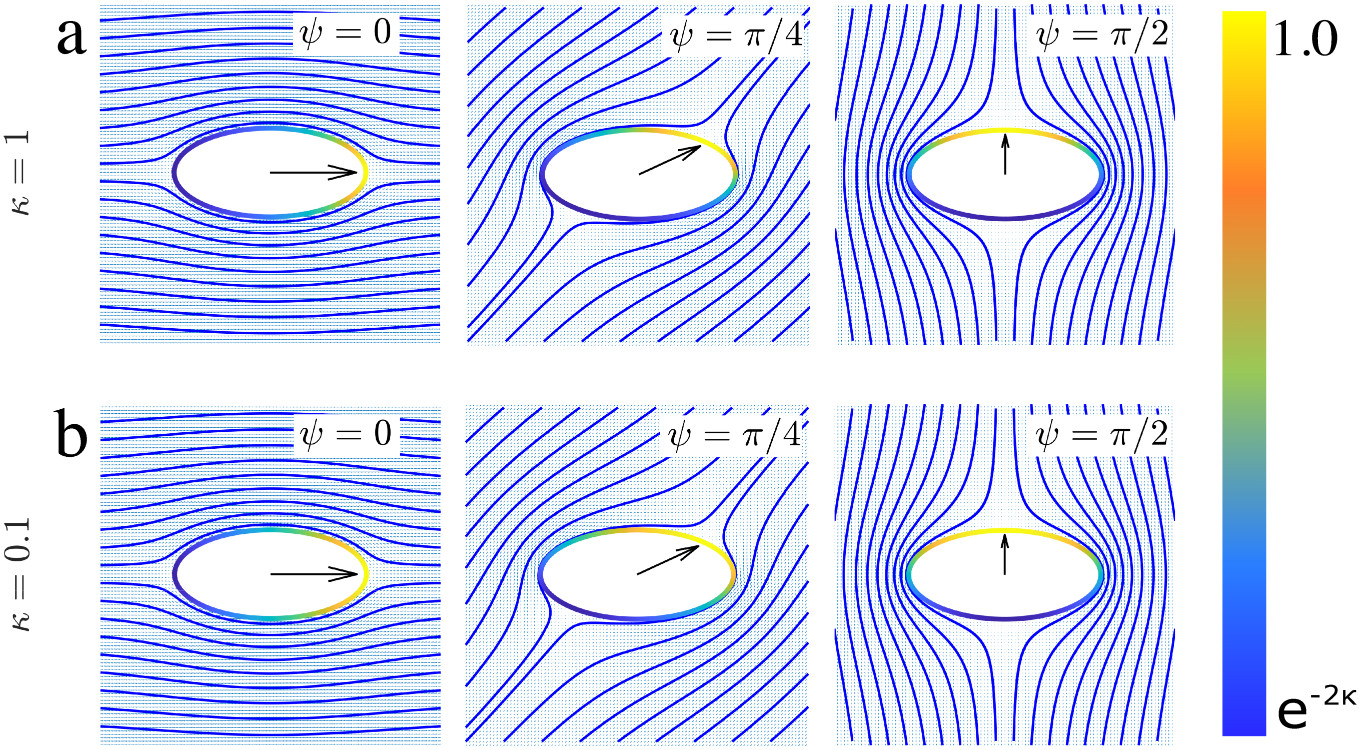

FIG. 2: Field lines of the field outside the cell, given three different orientations ψ of the applied field. Note that from the boundary conditions (Appendix B), the normal component of the electric field vanishes at the cell boundary. Sensor concentration $c(\nu)$ is also plotted as a color map. The concentration is plotted as $c(\nu)/c_{\max}$, where $c_{\max} = c_0 e^{\kappa}$. This normalization sets the maximum of the colorbar to 1 and the minimum to $e^{-2\kappa}$. (a) Field lines and sensor concentration when $\kappa = 1$. (b) Field lines and sensor concentration when $\kappa = 0.1$.

the cell's boundary with velocity $\mathfrak{u}$. We assume that $\mathfrak{u} = \mathfrak{m}\mathbf{E}_\parallel$, where $\mathfrak{m}$ is the electrophoretic mobility constant. This mobility constant can be positive or negative depending on the sensors' charge and the zeta potential of the cell surface [29]; we do not attempt to estimate $\mathfrak{m}$, but think of it as phenomenological and generally try to fit it from experimental data. The assumption that the velocity is proportional to the local electric field is reasonable since the cell's membrane is treated as non-conducting and the electric double layer is thin compared to the radius of curvature of the cell [29, 48]. Each sensor is labeled by its elliptic angle location ν_i. Transport of the density of sensors c along the contour can be derived by balancing the advective flux $c\mathfrak{u}$ with the diffusive flux. This flux balance captures the competition between sensor migration driven by the electric field, which tends to polarize the sensors, and diffusion, which tends to spread the sensors out [29, 30]. The transport of sensors is explained by the equation

$$c\mathfrak{u} = D\nabla_\parallel c, \tag{3}$$

where $\nabla_\parallel$ is the gradient along the membrane and D the sensor's diffusion coefficient. The density of sensors can only depend on their location on the boundary ν, so we can write Eq. (3) explicitly as:

$$c(\nu)\mathfrak{m}\mathbf{E}_\parallel = D\frac{1}{h_{\mu_0}}\frac{\partial c(\nu)}{\partial \nu}\hat{\boldsymbol{\nu}}. \tag{4}$$

The scale factor h_μ appears in this calculation from the expression of the gradient in the $\hat{\boldsymbol{\nu}}$ direction in elliptic coordinates. Substituting in Eq. (2) for $\mathbf{E}_\parallel$ and rearranging, the solution is proportional to the von Mises distribution [49]

$$c(\nu) = c_0 \exp\left[\kappa \cos\left(\nu - \psi\right)\right]. \tag{5}$$

Here, c_0 is a proportionality constant set to determine the total number of sensors. $\kappa = \mathfrak{m}E_0 a e^{\mu_0}/D = \mathfrak{m}E_0(R_1 + R_2)/D$ is the ratio between the rate of electromigration and diffusion (Péclet number [50]). If κ is larger, electromigration dominates diffusion, and the sensors are more concentrated (note the extent of the yellow region in Fig. 2a versus b). We often want to think about κ as a ratio between the strength of the applied electric field E_0 and some characteristic field scale, $1/\beta$, so we write $\kappa = \beta E_0$, where $\beta = \mathfrak{m}(R_1 + R_2)/D$. For circular cells with radius R_0 [30], we found a similar result of concentration proportional to $e^{\beta E_0 \cos(\theta - \psi)}$ in polar coordinates, with $\beta = \mu R_0/D$. (Note that μ here is not the elliptic radius!) Our result in Eq. (5) will more obviously limit back to this result if we define $\beta = \bar{\mathfrak{m}}\bar{R}/D$, where $\bar{\mathfrak{m}} = 2\mathfrak{m}$ and $\bar{R} = (R_1 + R_2)/2$. $c(\nu)$ is plotted in Fig. 2a–b in conjunction with the electric field lines.

We note that in our prior manuscript [30] we assumed $\mathfrak{u} = \mu\mathbf{E}_{0,\parallel}$, where $\mathbf{E}_0$ was the *applied* field and μ is a mobility constant. In this manuscript there is a subtle difference. Now, $\mathfrak{u} = \mathfrak{m}\mathbf{E}_\parallel$, where $\mathbf{E}_\parallel$ is the *local* electric field tangent to the cell boundary and $\mathfrak{m}$ is the mobility constant. For circular cells, either choice gives the same answer, but with a conventional factor of 2 between μ and $\mathfrak{m}$ (see Appendix A of [30]), but for elliptical cells, this is not the case. Therefore, we have chosen the more physically-realistic assumption $\mathfrak{u} = \mathfrak{m}\mathbf{E}_\parallel$.

The concentration of Eq. (5) gives the number of sensors per unit length of boundary; we will need to work with $\mathcal{P}(\nu)$, the probability density per elliptic angle ν. Changing variables, this can be found as

$$\mathcal{P}(\nu) = Z^{-1} c(\nu) h_{\mu_0}, \tag{6}$$

where

$$Z = \int_{\psi-\pi}^{\psi+\pi} c(\nu) h_{\mu_0} \mathrm{d}\nu. \tag{7}$$

(See Fig. S3 and Appendix E for more details.)

Maximum likelihood estimation and Fisher information

Following [30], we use maximum likelihood estimation to quantify the cell's estimate of the field's direction. We ask ourselves "What electric field direction maximizes the likelihood of observing a given probability distribution of sensors?" The likelihood function for N noninteracting sensors, each at elliptic angle ν_i, is given by

$$\mathcal{L}(E, \psi; \{\nu\}) = \prod_{i=1}^{N} \mathcal{P}(\nu_i), \tag{8}$$

however, the log-likelihood is easier to work with

$$\ln \mathcal{L} = \sum_{i=1}^{N} \left[\kappa \cos(\nu_i - \psi) + \ln h_{\mu_0}^{(i)} \right] - N \ln Z. \tag{9}$$

Here, $h_{\mu_0}^{(i)} = a\sqrt{(\cosh 2\mu_0 - \cos 2\nu_i)/2}$, where the superscript i acts as a label for sensor i. To minimize $\ln \mathcal{L}$, we differentiate, setting $\partial_\psi \ln \mathcal{L}|_{\hat{\psi}} = 0$ to get an expression that gives us the estimator $\hat{\psi}$

$$\frac{1}{N} \sum_{i=1}^{N} \kappa \sin(\nu_i - \hat{\psi}) = \frac{1}{Z} \frac{\partial Z}{\partial \psi}. \tag{10}$$

The integrals that define Z and $\partial_\psi Z$ on the right hand side of Eq. (10) have to be evaluated numerically in general, but have an analytical solution in the limit of near-circular cells (see Appendix G 1). In the special case of a circular cell, the elliptic angle ν_i tends to the polar angle θ_i, the right hand side of Eq. (10) equals zero, and the cell's prediction $\hat{\psi}$ of the true field angle ψ can be solved explicitly by the equation [30]

$$\tan \hat{\psi} = \frac{\sum_i \sin \theta_i}{\sum_i \cos \theta_i} \quad \text{(circular cells)}. \tag{11}$$

The Fisher information can also be derived from the log-likelihood by calculating $\mathcal{I} = \langle -\partial_\psi^2 \ln \mathcal{L} \rangle$ (see Appendix F for derivation):

$$\mathcal{I} = N\kappa^2 \left[\left\langle \sin^2(\nu - \psi) \right\rangle - \left\langle \sin(\nu - \psi) \right\rangle^2 \right]. \tag{12}$$

We can compute the averages in Eq. (12) numerically, $\langle \cdots \rangle = \int \cdots \mathcal{P}(\nu) \mathrm{d}\nu$. The Fisher information reveals how much information the cell would have about the field direction given a particular distribution of sensors. The Fisher information is crucial for quantifying the variability in the cell's estimate. Since the estimate $\hat{\psi}$ is periodic in nature, we characterize variability in the estimate with the circular variance $2(1 - \langle \cos(\hat{\psi} - \psi) \rangle)$, which will reduce to the ordinary variance in the limit where the deviation between $\hat{\psi}$ and ψ is small. The circular variance of $\hat{\psi}$ has a lower bound given by an extension of the Cramér-Rao bound (derived in Appendix D of [30])

$$2(1 - \langle \cos(\hat{\psi} - \psi) \rangle) \geq 2\left(1 - \sqrt{\frac{\mathcal{I}}{1 + \mathcal{I}}}\right) \tag{13}$$

or, equivalently, $\langle \cos(\hat{\psi} - \psi) \rangle \leq \sqrt{\mathcal{I}/(1 + \mathcal{I})}$. The lower bound for the circular variance becomes more accurate as number of sensors increases or the sensors become more polarized – in this limit, the inequality becomes an equality. We will compute the Fisher information $\mathcal{I}$ for an elliptical cell in order to determine the accuracy with which it can sense the field angle ψ.

Stochastic simulations

In addition to our analytic and numerical results, we also conduct stochastic simulations using randomly-generated configurations of sensors. We generate a configuration of N sensors for each of N_{cell} cells. The configurations were generated by the rejection sampling method, drawing N sensor positions independently from Eq. (6) [51]. Briefly, we propose a uniformly-distributed sensor location $\nu_i \sim \mathcal{U}([\psi - \pi, \psi + \pi])$, as well as $u_i \sim \mathcal{U}([0, 1])$. Then, we compute $p_i = \mathcal{P}(\nu_i)/\sup\{\mathcal{P}(\nu)\}$. If $p_i > u_i$, then the proposed ν_i is selected as one of the sensor positions. Otherwise the proposal is rejected. This process is repeated until N sensors are generated.

If we assume the cells are estimating the field by maximizing the likelihood, the cell's estimate $\hat{\psi}$ is calculated by numerically finding the $\hat{\psi}$ that maximizes the log-likelihood, using Eq. (9). We use the Nelder-Mead simplex algorithm (MATLAB's fminsearch) [52]. We will also sometimes assume cells choose a direction as the vector sum of unit normals pointing from the sensor locations (Eq. (17)).

During our simulations (for both MLE and vector sum), we fix the the average of the cell semi-major and minor axes as $\bar{R} = 20\ \mu$m (typical keratocyte radius from Fig. 4a of [53]). If λ is fixed, it is fixed at

$\lambda = 3$, the reasonable upper limit for aspect ratio of a keratocyte; see Fig. 4b of [53]). R_2 was selected so $(R_1 + R_2)/2 = (1 + \lambda)R_2/2 = \bar{R}$ remains fixed (see Appendix A).

RESULTS

Accuracy of galvanotaxis depends on cell orientation, aspect ratio, and Péclet number κ

The Fisher information $\mathcal{I}$ tells us how much information the cell has about the electric field direction from its sensor distribution. It can be hard to draw intuition from Eq. (12) as it must be evaluated numerically. Fortunately, in the limit of nearly circular cells with sensors whose motion is dominated by diffusion (small κ), the Fisher information $\mathcal{I}$ simplifies to (see Appendices G 1-G 3)

$$\mathcal{I} = N\kappa^2 \left(\frac{1}{2} + \zeta_0 \cos 2\psi \right). \tag{14}$$

The aeolotropic constant ζ_0 characterizes the anisotropic contribution to the Fisher information. In other words, it accounts for the cell's deviation from a circle. It is a function of the aspect ratio λ,

$$\zeta_0(\lambda) = \frac{1}{8} \frac{\lambda^2 - 1}{\lambda^2 + 1}. \tag{15}$$

ζ_0 is positive for all aspect ratios $\lambda \geq 1$, and ζ_0 goes to zero for circular cells and $\zeta_{\max} \to 1/8$ for infinitely elliptical cells e.g. one-dimensional lines (Fig. 3).

Eq. (14) predicts that the cell's amount of information varies depending on its orientation with respect to the field, with the Fisher information $\mathcal{I}$ maximal when the field is along the major axis and minimal when the field is along the minor axis. From the perspective of the model, this is not surprising. We see in Fig. 2 that the sensors are more concentrated when the cell's long axis is parallel to the field. Therefore we expect more information about the cell's orientation in this configuration. How much information does the cell have when the field is parallel to the cell ($\psi = 0$) versus perpendicular to the cell ($\psi = \pi/2$)? Because ζ_0 is at most 1/8, we can see from Eq. (14) that the largest the ratio between the maximum information at $\psi = 0$ and minimum at $\psi = \pi/2$ is $\mathfrak{R}_{\max} = 5/3$. This corresponds to an at most $\sim 67\%$ increase in information in the "best" orientation versus the "worst" orientation. We note that this result depends on Eq. (14), which is only valid in the limit of near-circular cells, where λ is not too far from unity. However, we see in Fig. 4b that Eq. (14) is a suitable approximation for the full solution in Eq. (12) even out to $\lambda \approx 10$ if $\kappa \approx 0.5$. So for any reasonable cell shape, we are confident in Eq. (14) as long as κ is sufficiently small.

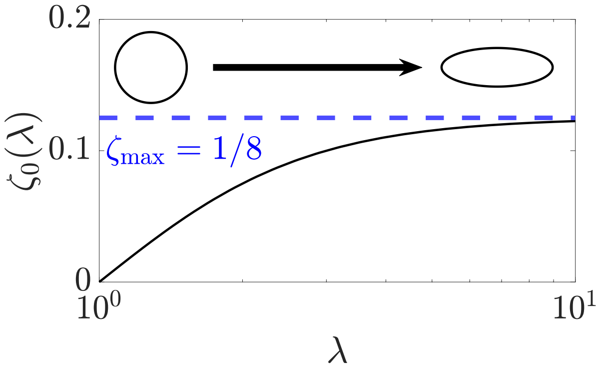

FIG. 3: Aeolotropic constant ζ_0 as a function of aspect ratio λ; the constant increases and saturates as a cell becomes more elliptical, approaching its maximum of 1/8.

The Fisher information, combined with the bound of Eq. (13), tells us the minimum possible circular variance for an unbiased estimate of the direction ψ. We plot in Fig. 4a how the circular variance $2(1 - \langle\cos(\hat{\psi} - \psi)\rangle)$ varies with the Péclet number κ. Unsurprisingly, we see that $2(1 - \langle\cos(\hat{\psi} - \psi)\rangle)$ decreases with increasing κ and increasing number of sensors N. In Fig. 4, we show the bound of (13) using both the analytical solution for the weak-field Fisher information approximation Eq. (14) (dashed line), and a full numerical solution to the Fisher information (solid line), and stochastic simulations (symbols). The small-κ approximation deviates from the numerical solution and stochastic simulations at large κ, as expected.

We see in Fig. 4a that the simulations generally agree with the full numerical solution (solid lines) – but there is a small systematic deviation at very low κ ($\kappa \ll 1$). In this regime, the simulations yield slightly higher values than what the theory predicts. This behavior is expected, and similar to what we found in [30]; see that paper's Fig. 2. Eq. (13) is a lower bound for the circular variance, so it is always possible that the circular variance of the maximum likelihood estimator is above this bound. We found previously that for circular cells [30], the circular variance of the maximum likelihood estimator converges onto our modified Cramer-Rao bound in the limit of large amount of information (large κ and large N). (This convergence is guaranteed because that the maximum likelihood estimator is asymptotically efficient [54].)

In Fig. 4b, we see that circular variance $2(1 - \langle\cos(\hat{\psi} - \psi)\rangle)$ changes only slightly as aspect ratio increases while holding κ constant. Changing aspect ratio λ while holding κ constant means that $(R_1+R_2)/2$ is held constant while $\lambda = R_1/R_2$ is changing, meaning that as a cell simultaneously becomes longer and thinner. This sort of change leads to only small differences in circular variance. The sign of the change of circular variance with λ will depends on ψ, since the Fisher information can increase or decrease with aspect ratio depending on the sign of $\cos 2\psi$ (Eq. (14)); we have plotted Fig. 4b with the field at angle $\psi = \pi/3$, and the long axis of the

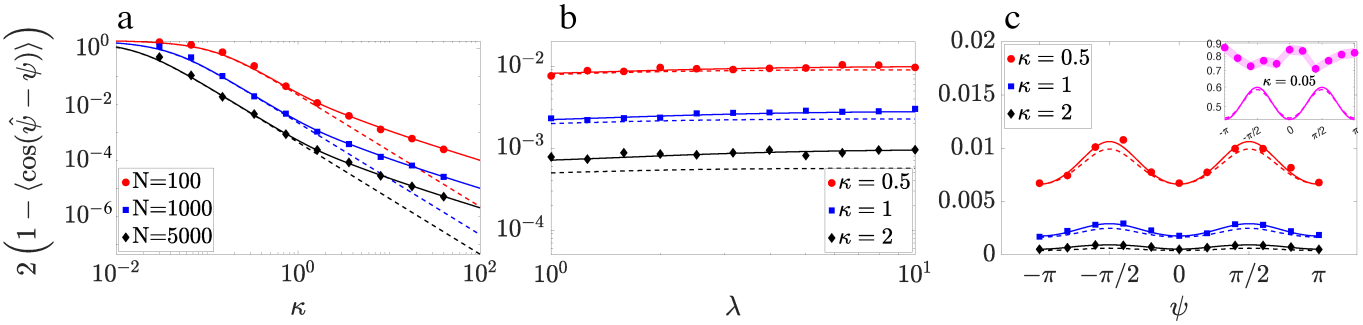

FIG. 4: Circular variance changes as a function of the Péclet number κ, aspect ratio λ, field direction ψ, and number of sensors N. Solid lines are given by Eq. (13), which was calculated by numerically computing the Fisher information of Eq. (12) and inserting it into Eq. (13). Dashed lines are the analytic approximation of Eq. (14). Symbols are stochastic simulation averaged over 500 cells (a) or 1000 cells (b, c). Error bars (standard error of the mean) are on the order of the symbol size. (a): Circular variance as a function of the Péclet number κ, plotted for various values of number of sensors N. The aspect ratio $\lambda = 3$. The field angle relative to the long axis of the cell is $\psi = \pi/3$. (b): Circular variance as a function of the aspect ratio λ, plotted for various values of κ. The number of sensors is $N = 1000$. The field angle is $\psi = \pi/3$. (c): Circular variance as a function of the true field direction ψ, plotted for various values of κ. The number of sensors is $N = 1000$. The aspect ratio is $\lambda = 3$. The inset plots same thing as (c) but for $\kappa = 0.05$. Here, the shaded region around the simulation symbols represent the error bars, which is the standard error of the mean.

cell, as always, along the x-direction.

Fig. 4c reveals that the error in the cell's measurement depends on its orientation relative to the field, as we expected from the discussion of Eq. (14). We see that the circular variance is minimal when the field is pointed along the cell's major axis ($\psi = 0$) where there is the most information, and maximal along the minor axis where there is the least information ($\psi = \pi/2$). All of the plots in the main body of Fig. 4c, which are in the range $\kappa \geq 0.5$, show good agreement between simulations and the bound of Eq. (13) (symbols near-exactly overlapping with the solid line). However, as we mentioned above discussing Fig. 4a, we know that the bound is no longer tight in the limit of smaller κ – the circular variance will exceed the bound. We plot this limit in the inset of Fig. 4c. Surprisingly, not only does the circular variance of the maximum-likelihood estimate of the simulations exceed the bound, but the maximal circular variance occurs at $\psi = 0$, where the bound is minimal. This means that, in this limit of very small fields, cells with their long axis perpendicular to the field will have lower error in measuring the field angle. The origin of this effect is not clear, and we explore it further below.

Modeling keratocytes as ellipses can minimize semi-minor axis variance perpendicular to the electric field under weaker field strengths

In Fig. 4c, we have seen that, depending on κ, cells' best orientation could be *either* with their long axis parallel to the field or perpendicular to the field. Which of these limits is relevant for real cells? We will fit our model to the case of fish keratocytes, a well-studied model system for cell locomotion and galvanotaxis [16, 40, 53, 55, 56]. We fit our model, assuming the weak-field limit of Eq. (14), to data measuring keratocyte directionality as a function of electric field strength [57] (details in Appendix H). Directionality measures the average angle between the cell's velocity and the applied electric field; we think of the cell's velocity as a proxy for its estimate of the field direction, so the directionality is just $\langle \cos(\hat{\psi} - \psi)\rangle$. We can then fit the directionality data to get the parameters of our model by using the approximation $\langle \cos(\hat{\psi} - \psi)\rangle \approx e^{-\mathcal{I}^{-1}/2}$ (Appendix H). We note that our formula for $\mathcal{I}$ does not separately depend on N and κ but only on their product $N\kappa^2 = N\beta^2 E_0^2$, so we cannot separately fit N and β. We define, as in [30], $\gamma^2 = N\beta^2/2$. $1/\gamma$ is a characteristic field strength. Then, Eq. (14) can be written as $\mathcal{I} = \gamma^2 E_0^2(1 + 2\zeta_0 \cos 2\psi)$. We choose $\lambda = 3$ as a rough estimate for keratocytes [53], which sets the aeolotropic constant $\zeta_0(3) = 0.1$. As keratocytes typically migrate with their long axis aligned perpendicular to the electric field [16, 55], $\psi = \pi/2$, and the Fisher information for keratocytes can be simplified to

$$\mathcal{I} = 0.8\gamma^2 E_0^2 \quad (\text{keratocytes} \perp \text{to field}). \tag{16}$$

If we fit experimentally-measured directionality as a function of the electric field using Eq. (16) and $\langle \cos(\hat{\psi} - \psi)\rangle \approx e^{-\mathcal{I}^{-1}/2}$ (see Appendix H and Fig. S5), we find $\gamma = 3.4 \times 10^{-3}$ mm/mV.

Do keratocytes have a preferred orientation in which they sense more accurately? Fig. 5b plots the circular variance as a function of field angle using our keratocyte estimate for γ at a typical field strength of $E_0 = 150$ mV/mm. We see that while the bound given by Eq. (13) predicts the minimal variance at $\psi = 0$, stochastic simulations predict the opposite trend – the minimal circular variance is at $\psi = \pi/2$. (This result does not depend on the number of sensors N as long as we hold the magnitude of the Fisher information constant by keeping $\gamma^2 = N\beta^2/2$ fixed; see Fig. S6 in Appendix I.) To illustrate where this transition in preferred axis happens, we plot the circular variance at

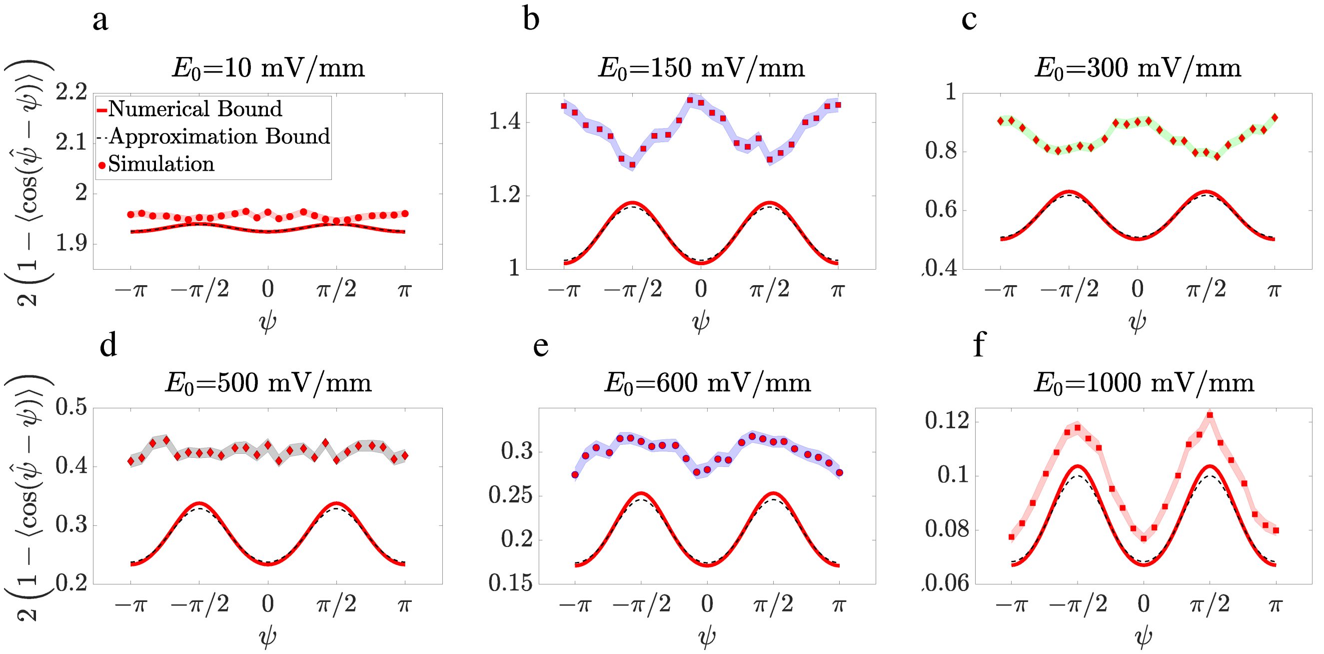

FIG. 5: Circular variance as a function of the field orientation ψ for keratocytes using MLE. The aspect ratio $\lambda = 3$, $\gamma = 3.4 \times 10^{-3}$ mm/mV, and the number of sensors $N = 1000$ are kept constant. Solid red lines are given by Eq. (13), which was calculated by numerically determining Fisher information of (12), and plugging back into Eq. (13). Dashed black lines are using the analytic approximation Eq. (14). Symbols are stochastic simulation averaged over 5000 cells (5a is averaged over 50000 cells). Shaded regions around the symbols represent the standard error of the mean.

$\gamma = 3.4 \times 10^{-3}$ mm/mV for increasing field strengths in Fig. 5a-f. We can see a wide variety of trends, ranging from cells all having near-uniformly distributed estimators (circular variance ≈ 2) at $E_0 = 10$ mV/mm to cells having minimal error when perpendicular to the field ($E_0 = 150, 300$ mV/mm) transitioning to a flat dependence on angle ($E_0 = 500$ mV/mm) and eventually seeing the trend predicted by the Fisher information at larger field ranges (1000 mV/mm). This range of field strengths is the experimentally relevant range. It goes from the weakest field strengths that cells types such as neural crest cells have responded to ($E_0 = 10$ mV/mm [22]) to the strongest fields typically used in galvanotaxis experiments ($E_0 = 1000$ mV/mm [31]). Note the the difference between the peaks and troughs of the circular variance lower bound and simulations become smallest at low fields ($E_0 = 10$ mV/mm), high fields ($E_0 = 1000$ mV/mm), and the transition ($E_0 = 500$ mV/mm).

The result of Fig. 5 is somewhat dramatic. The trend in circular variance of the maximum likelihood estimate can be the *opposite* of the bound predicted by the Fisher information. This is surprising! We certainly initially expected that even if the circular variance exceeded the bound, it would follow a similar trend. We do not have a clear explanation for why this occurs. One possibility is that this behavior arises due to some odd property of the maximum likelihood estimator (or our numerical evaluation of the estimator) – but we will see in the next section that a more physically plausible estimator also has lower variance when the field is perpendicular to the cell's long axis.

Vector sum is a biased but plausible sensing strategy

We have used the maximum likelihood estimation approach in our earlier results because it is asymptotically efficient. In the limit of large numbers of observations, it should reach the Cramer-Rao bound. However, as a model for a biological organism, it has the clear downside of being extremely complicated to compute since cells presumably do not have Nelder-Mead optimization easily available. We found in [30] that the maximum likelihood estimator for a *circular* cell is the direction of the vector sum of vectors pointing to each sensor. This estimate could be easily computed if the cell exerts a protrusive force localized at each sensor, pointing normally outward (see Appendix K of [30]). This scheme is physically plausible, and consistent with the idea that local charge regulates protrusion [58]. In this section, we study the properties of cells that estimate directions with vector sum, taking the sum of the unit normals $\hat{\boldsymbol{\mu}}_i$ for each sensor i pointing out from the ellipse,

$$\bar{\boldsymbol{\mu}} = \frac{1}{N}\sum_{i}^{N} \hat{\boldsymbol{\mu}}_i, \tag{17}$$

$$\hat{\psi}_{\mathrm{VS}} = \arctan\left(\bar{\mu}_y/\bar{\mu}_x\right). \tag{18}$$

Unlike our results for circular cells, for an ellipse, the

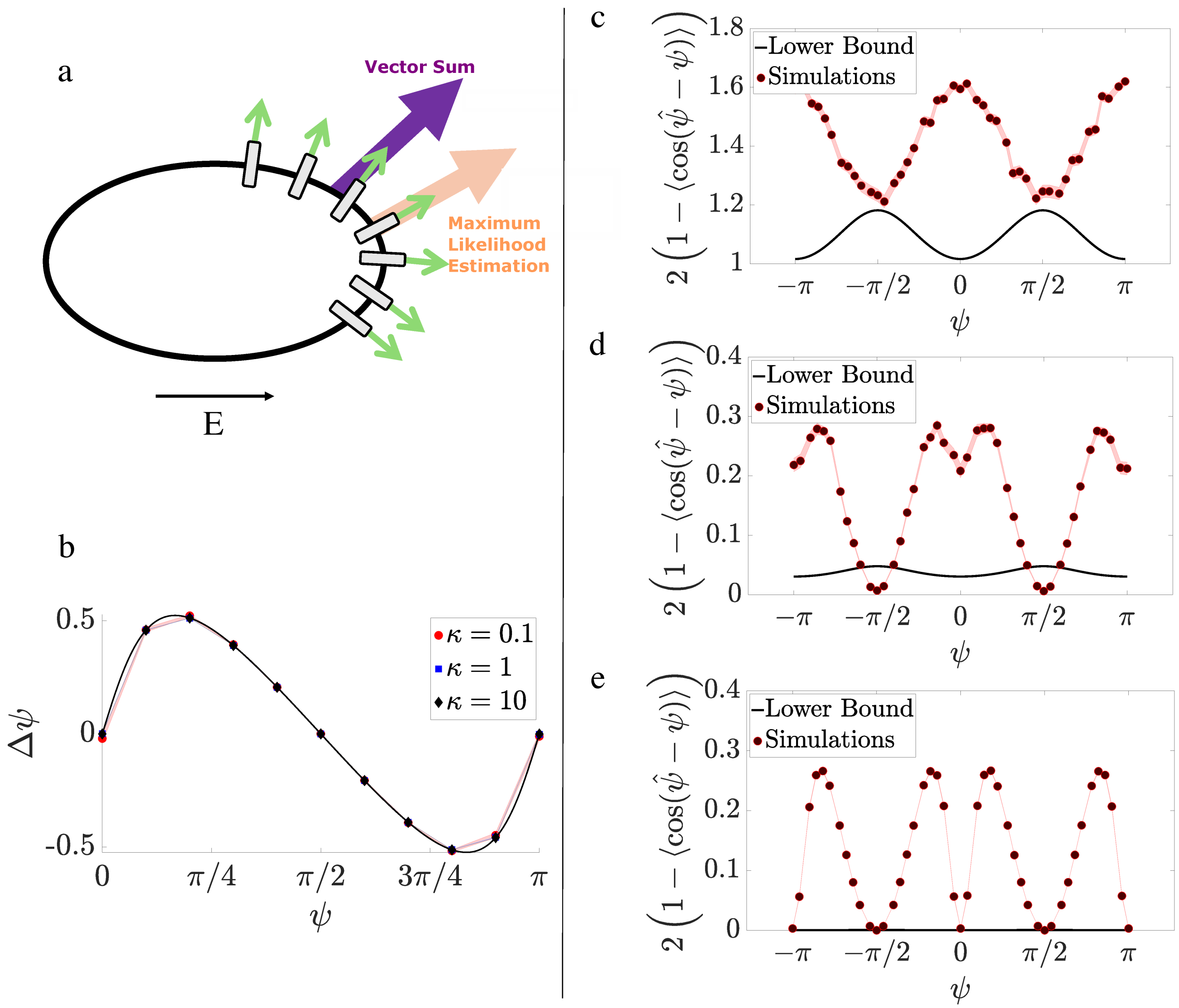

FIG. 6: (a): Schematic showcasing the bias that vector sum introduces relative to MLE. (b): Vector sum as a function of field angle. Symbols are simulation, averaged over 500 cells. Shaded area between the symbols indicates standard error of the mean. Solid lines are numerical calculation of Eq. (19). Here, we have $N = 10000$ and $\lambda = 3$. $\langle\hat{\psi}_{\mathrm{VS}}\rangle$ is computed here by first computing $\hat{\psi}_{\mathrm{VS}}$ for each cell and then averaging. (c): Circular variance plot for keratocytes calculated using vector sum. $N = 10000$, $\gamma = 3.4\times10^{-3}$ mm/mV, and $\kappa \approx 5\times10^{-3}$. Black line is the lower bound from Eq. (13). Simulations are represented by the symbols and are averaged over 5000 cells. Shaded region are standard error of the mean. (d): Circular variance plot for keratocytes calculated using vector sum. $N = 10000$, $\gamma = 3.4\times10^{-3}$ mm/mV, and $\kappa \approx 5\times10^{-2}$. Black line is the lower bound from Eq. (13). Note that the simulations drop below the lower bound, as the lower bound assumes an *unbiased* estimator, which is not true for the vector sum. Simulations are represented by the symbols and are averaged over 500 cells. Shaded region are standard error of the mean. (e): Circular variance plot for keratocytes calculated using vector sum. $N = 10000$, $\gamma = 3.4\times10^{-3}$ mm/mV, and $\kappa \approx 5\times10^{-1}$. Black line is the lower bound from Eq. (13). Simulations are represented by the symbols and are averaged over 500 cells. Shaded region indicates standard error of the mean.

vector sum estimator $\hat{\psi}_{\mathrm{VS}}$ and the maximum-likelihood estimate $\hat{\psi}_{\mathrm{MLE}}$ are not identical. In fact, we see in Fig. 6a and 6b that the vector sum estimate is biased. In Fig. 6b, we plot the difference between the vector sum estimate, averaged over 500 simulated cells, and the true field orientation, $\Delta\psi = \langle\hat{\psi}_{\mathrm{VS}}\rangle - \psi$ as a function of the true field orientation. We find that the bias in the vector sum estimator vanishes, $\Delta\psi = 0$, if the field is pointing along the long axis ($\psi = 0, \pi$) or the short axis ($\psi = \pi/2, 3\pi/2$), and is a maximum in between these orientations. We see that $\langle\hat{\psi}_{\mathrm{VS}}\rangle$ does not point precisely in the true direction ψ but has a consistent bias toward the minor axis. This bias does not appear to depend on κ (Fig. 6b). In addition to the simulations, we also calculate $\hat{\psi}_{\mathrm{VS}}$ from the average of the unit normal,

$$\langle\hat{\boldsymbol{\mu}}\rangle = \int_{\psi-\pi}^{\psi+\pi} \hat{\boldsymbol{\mu}}\mathcal{P}(\nu)\mathrm{d}\nu, \qquad (19)$$

and, in a slight abuse of notation, $\hat{\psi}_{\mathrm{VS}} =$

$\arctan(\langle\hat{\mu}_y\rangle/\langle\hat{\mu}_x\rangle)$. We can compute this integral analytically, finding that $\langle\hat{\mu}_x\rangle = \mathcal{A}(\kappa)\sinh\mu_0\cos\psi$ and $\langle\hat{\mu}_y\rangle = \mathcal{A}(\kappa)\cosh\mu_0\sin\psi$ with $\mathcal{A}(\kappa) = 2\pi a I_1(\kappa)Z^{-1}$, which is a function that depends on κ and cell shape. $I_1(\kappa)$ is a modified Bessel function of the first kind. Since the aspect ratio of the cell is $\lambda = \cosh\mu_0/\sinh\mu_0$ (Appendix A), we see that the vector sum points in the direction $(\cos\psi, \lambda\sin\psi)$. This means that the vector sum becomes more biased to be parallel to the short axis for more elongated cells. Our formula also shows that the bias is solely geometrical. It does not depend on κ (Fig. 6b). (A minor technical note: our finding that $\Delta\psi \neq 0$ does not, strictly speaking, tell you that the estimator must be biased in a periodic sense [30, 59]. However, we do also find that $\langle\sin(\hat{\psi}_{\mathrm{VS}} - \psi)\rangle$ is nonzero.)

How accurate is the vector sum? If cells compute using the vector sum, are they better at measuring when parallel to the field or perpendicular to the field? We use parameters appropriate to the keratocytes, as we did in Fig. 5, and compute the circular variance as a function of the field angle (Fig. 6c). We find that vector sum also predicts that the cell has the smallest variance when the long axis is perpendicular to the field ($\psi = \pm\pi/2$). In fact, for $\psi = \pm\pi/2$, the cell is nearing our bound Eq. (13) (Fig. 6c). However, we note that the vector sum is not constrained by this bound – it could give circular variances below the bound, since we derived Eq. (13) under the assumption of an unbiased estimator. When κ is increased from the physiologically relevant value of $\kappa \approx 5 \times 10^{-3}$ (Fig. 6c) by a factor of 10 (Fig. 6d), this corresponds to increasing the field strength from 150 mV/mm to 1500 mV/mm. However, even at this high electric field, the variance of the vector sum is minimal when the cell's long axis is perpendicular the field, though there is a dip in the circular variance curve near $\psi = 0$. This should be contrasted to Fig. 5, in which a similar change in magnitude of electric field completely inverts the trend. We also note that in Fig. 6d, the vector sum circular variance may fall below the bound, as is expected given the biased estimation – our extended Cramér-Rao bound [30] was derived under the assumption of an unbiased estimator $\hat{\psi}$.

In Fig. 6e, κ is increased further by two orders of magnitude from the case of Fig. 6c. Though this limit is likely no longer experimentally relevant, we see that increasing κ magnifies the difference in sensing accuracy between having a cell with one of it principal axis aligned with the field versus not having one aligned. In this limit, the circular variance is at a minimum when the field is either along the long *or* the short axis of the cell. We believe this reflects the bias in the vector sum strategy. When κ becomes large, the error bound from stochasticity shrinks relative to the size of the bias, and the systematic errors of order ~ 0.5 radians shown in Fig. 6b are large relative to the variability from stochastic sensor locations. When this bias is relevant, as in Fig. 6e, there are strong consequences for not sensing the field along one of the principal axes, as the error can be orders of magnitude higher off of any main axis.

Cell shape expands parallel or perpendicular to the field, depending on sensor mobility

Keratocytes migrate with their long axis perpendicular to the electric field. This could be because they sense more accurately along the short axis, which our circular variance results may suggest, and earlier work has also assumed [60]. Another possibility is that the keratocyte orientation to the field is a downstream effect of the cell creating protrusions towards the electric field and then elongating perpendicular to the field. Both scenarios hint at a link between sensor redistribution and cell shape and orientation. Up to this point, we have only measured the cell's response to an electric field while considering its fixed elliptical shape. Given that cells may change shape in response to electric fields [61, 62], we want to link sensing mechanics with cell deformation and find out whether cells tend to expand parallel to the field or perpendicular to the field.

We build an initial simple model of cell shape coupled with field sensing by describing the cell shape as arising from radial protrusions that are graded around the cell boundary [40]. As we discussed in the vector sum section, our idea is that the cell creates small protrusions perpendicular to its outer edge in areas where there is a high concentration of nearby sensors. As a result, cell direction and shape are controlled by protrusions normal to the boundary [40, 53]. We will assume (to make a few later calculations simpler) that the cell is near-circular. We can then describe the cell boundary by the radius function $\mathcal{R}(\theta, t)$ in polar coordinates (Fig. 7a) [42, 63, 64], which can be expanded by Fourier series

$$\mathcal{R}(\theta, t) = \mathcal{R}_0 + \delta\mathcal{R}(\theta, t) = \mathcal{R}_0 + \sum_{-\infty}^{\infty} \rho_n(t) e^{in\theta}. \qquad (20)$$

The $n = 0, \pm 1$ terms are implicitly excluded from the sum. The $n = 0$ mode corresponds to a uniform expansion/contraction of the cell, and the $n = \pm 1$ modes correspond to simple translational motion, which we include by assuming that the cell is initially traveling with a constant speed. We assume the force balance for the cell interface can be given by

$$\tau\mathcal{V}(\theta, t) = \eta\mathcal{K}(\theta, t) + \alpha\left(c(\theta, t) - c^*\right), \qquad (21)$$

where $\mathcal{V}$ is the normal velocity of the cell interface, $\mathcal{K}$ is the interface's curvature, and c is the local concentration of sensors. τ is a friction coefficient, i.e. $-\tau\mathcal{V}$ is the frictional drag force per unit length. The term proportional to the interface curvature tends to minimize the cell perimeter (i.e. it reflects a line tension) – the coefficient η has units of force. The $\alpha\left(c(\theta, t) - c^*\right)$ term says that, if $\alpha > 0$, the cell generates normally outward protrusions where the sensor concentration is above a

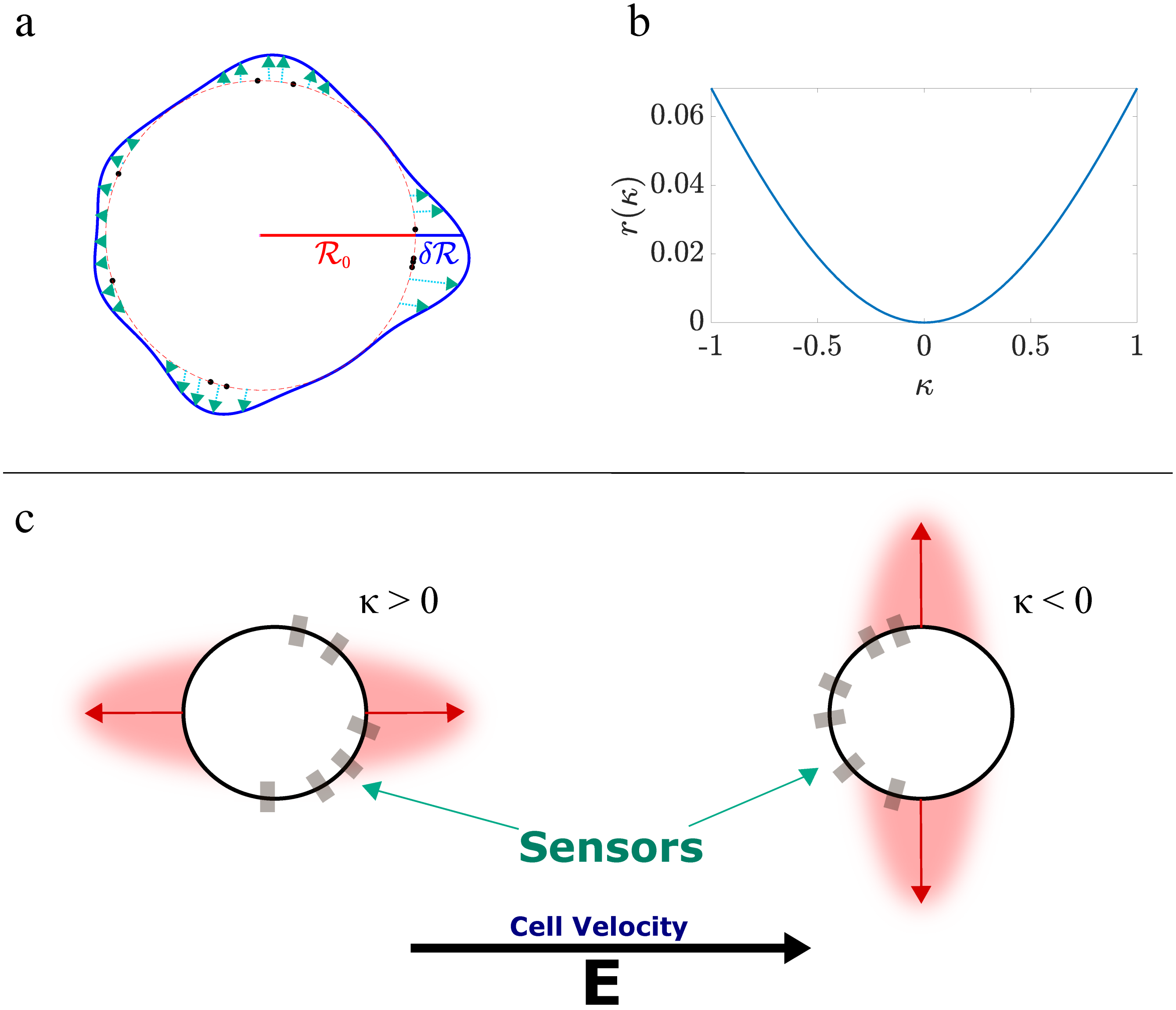

FIG. 7: (a): Schematic of cell whose protrusions occur at the sensor locations (black points). The radius $\mathcal{R} = \mathcal{R}_0 + \delta\mathcal{R}$. (b): Plot of $\mathfrak{r}(\kappa)$ showing that it is nonnegative for both positive and negative κ. (c): Cell with either sensors transported parallel to the applied electric field ($\kappa > 0$), causing the cell to expand parallel to the field, or with sensors transported opposite to the applied electric field ($\kappa < 0$), causing the cell to expand perpendicular to the field. Cells in (c) are migrating towards the electric field.

threshold concentration, $c > c^*$, and contractions elsewhere. Together these assumptions are essentially those of the mechanical models in, e.g. [41, 65, 66]. Similar equations of motion can be derived for interfaces in reaction-diffusion dynamics [67].

We are primarily interested in whether the shape expands parallel to or perpendicular to the field – this is information that is encoded in the $n = \pm 2$ Fourier modes. Following [42] and expanding the normal velocity $\mathcal{V}$ and the curvature $\mathcal{K}$ in terms of the Fourier modes, we can find an equation of motion for the $n = \pm 2$ modes,

$$\frac{\mathrm{d}\rho_{\pm 2}}{\mathrm{d}t} = -\bar{\eta}\rho_{\pm 2} + \frac{\bar{\alpha}}{2\pi}\int_{\psi-\pi}^{\psi+\pi} \mathrm{d}\theta\, c(\theta, t) e^{\mp i 2\theta}, \qquad (22)$$

where $\bar{\eta} = 3\eta\mathcal{R}_0^{-2}\tau^{-1}$ and $\bar{\alpha} = \alpha\tau^{-1}$. Essentially, this equation reflects a balance of the line tension trying to make the cell more isotropic ($\bar{\eta}$ term, which decreases the amplitude of this Fourier mode) and the distribution of protrusion around the cell boundary in the $\bar{\alpha}$ term, which could make the cell more anisotropic. We are primarily interested in how the cell tends to break symmetry, whether it elongates parallel to or perpendicular to the field, so we will start by assuming that the cell is near-circular and so we use the formula for $c(\theta, t)$ appropriate for a circle. In this limit, Eq. (5) becomes $c(\theta) = c_0 e^{\kappa \cos(\theta - \psi)}$. We will choose the normalization constant c_0 so that the concentration integrates to 1, i.e. $c(\theta, t) = \frac{e^{\kappa(t)\cos(\theta-\psi)}}{2\pi I_0(\kappa(t))}$. (This absorbs the total number of sensors into the prefactor α.) Calculating the integral from Eq. (22) gives us

$$\frac{\mathrm{d}\rho_{\pm 2}}{\mathrm{d}t} = -\bar{\eta}\rho_{\pm 2} + \frac{\bar{\alpha}}{2\pi}\frac{I_2(\kappa)}{I_0(\kappa)}e^{\mp i2\psi}. \tag{23}$$

We then predict that at steady state, the Fourier modes settle to

$$\rho_{\pm 2} = \frac{\bar{a}}{2\pi}\frac{I_2(\kappa)}{I_0(\kappa)}e^{\mp i2\psi}, \tag{24}$$

where $\bar{a} = \bar{\alpha}/\bar{\eta}$. Moving back to real space, if we only include the $n = \pm 2$ Fourier modes, we then see how the cell's radius deviates from R_0 as

$$\begin{aligned} \delta\mathcal{R}(\theta) &= \rho_2 e^{i2\theta} + \rho_{-2}e^{-i2\theta} && (25) \\ &= \frac{\bar{a}}{2}\mathfrak{r}(\kappa)\cos[2(\theta-\psi)], && (26) \end{aligned}$$

where $\mathfrak{r}(\kappa) = \dfrac{2}{\pi}\dfrac{I_2(\kappa)}{I_0(\kappa)}$. Eq. (26) shows that, if $\alpha > 0$ ($\bar{a} > 0$), the cell will expand symmetrically along the field direction (Fig. 7c). Changing the electric field strength (changing κ) will change the magnitude of this expansion, but not its sign, as $\mathfrak{r}(\kappa)$ does not change sign when κ varies (Fig. 7b). We have so far assumed that $\alpha > 0$ implicitly by considering the mobility $\mathfrak{m}$ as nonnegative. This is a remnant of our earlier work where we assumed that sensors led to a net outward protrusion [30]. If the sensors are transported in the direction of the electric field, as we've illustrated in Fig. 1, net forces in the direction of the sensors will push the cell in the direction of the field. However, there is no constraint that our mobility $\mathfrak{m}$ (and subsequently κ) must be positive [29]! If sensors are instead transported to the *back* of the cell ($\mathfrak{m} < 0$), all of our earlier results will still hold – the results on Fisher information, etc. are insensitive to the sign of κ. However, if the sensors are instead at the back of the cell, the "vector sum" must have the opposite sign – the cell needs to generate contractile force where the sensors are highly concentrated. Therefore, for sensors that are swept to the back of the cell, we should have a negative value of α, and thus, cells will expand perpendicular to the field (Fig. 7c). This suggests that one possible interpretation of the observation that many cells tend to galvanotax perpendicular to the field is that they may have sensors that are swept to the cell rear.

We note that there are many caveats on our analysis here. The first is that cell shape is not just influenced by this radial protrusion, but also by any pre-existing cell polarity. Keratocytes, for instance, are elongated whether or not there is a field applied, and this elongated shape may arise from a wide variety of different models, independent of the field [53, 65, 68]. Our calculation essentially describes whether or not we would expect a net tendency for the cell to elongate perpendicular to the field. A second caveat of this calculation is that, to get an analytically tractable answer, we have restricted ourselves to assuming $c(\theta)$ is given by the steady-state limit for a circular cell. A more rigorous approach would be to initialize the cell with a uniform concentration of sensors, apply a field, and solve for the coupled transport of the sensors, shape change of the cell, and the change in the external field due to cell shape change in tandem. This is a much more complicated problem, and not within the scope of the current work.

DISCUSSION

Are cells better sensors of an electric field with long axis parallel to the field or perpendicular to the field? We find a fairly complicated answer. Figs. 5 and 6 show that the best choice depends both on the strength of the electric field, with the choice switching within the typical field range of 10-1000 mV/mm, and whether a cell estimates the field direction with a maximum likelihood estimation (likely difficult to compute) or a vector sum (plausible to compute).

Many groups have studied the fundamental physical limits of measurement accuracy of chemotaxis and chemosensing [39, 69–75]. Often, this work implicitly assumes that the cell can compute a maximum likelihood estimate – an estimate that may be physically intractable for the cell to compute due to its complexity. Our related work on galvanotaxis shows that simple, physically-plausible estimators like the vector sum may be biased for cells that don't have circular symmetry. This bias, however, is limited if cells' long axes are perpendicular or parallel to the field.

Many cell types migrate in an electric field with their long axis perpendicular to the field, including keratocytes, fibroblasts, multipotent mesenchymal stem cells, endothelial progenitor cells, neurons, neural crest cells, etc. [16, 55, 76–83], though *Dictyostelium discoideum* is a notable exception [84]. Do cells orient this way because it gives them a benefit during galvanotaxis [60]? This is plausible – there may be large increases in accuracy if cells are correctly oriented, especially if they are using the vector sum estimator (Fig. 6d). However, cells may also just naturally travel with their long axis parallel to their direction of polarity even in the absence of field – as keratocytes do. The most dramatic example of cell reorientation and shape change is Schwann cells, which would normally migrate with the long axis parallel to their direction of travel in the absence of a field, switch orientation to have the long axis perpendicular when in the presence of an electric field [85].

A second possibility explaining why cells tend to migrate with long axes perpendicular to the field is that this orientation occurs as a side effect of a mechanism where sensors drive protrusion. Our results show that a cell would expand parallel to the field if the sensors are in the front of the cell ($\kappa > 0$), and expand perpendicular to the field if the sensors are at the back of the cell ($\kappa < 0$). If this simple mechanism is reasonable, cell shape would directly indicate whether sensors localize to the cell front or cell back. Because Schwann cells [85] and MDCK cells [43] expand perpendicular to an applied field but do not have this orientation in the absence of field, our model would predict that they have sensors that localize to the cell back.

Our results in Fig. 4 show something somewhat disturbing and interesting for theorists of fundamental limits: the maximum likelihood estimator has a circular variance that is not only larger than our modified Cramer-Rao bound, but which has an *opposite* trend to the bound at small field strengths. While it is well known that the maximum likelihood estimator is only efficient (reaching the Cramer-Rao limit) in the limit of large numbers of samples [54] (here, large numbers of sensors), it is striking that the Fisher information can be completely misleading. Within our calculations, the Fisher information is always maximal when the electric field is oriented parallel to the cell's long axis. However, the maximum likelihood estimator's variance can be maximal in this circumstance – in other words, the variance of the maximum likelihood estimator is not even a monotonic function of the Fisher information. This result may encourage some revisiting of earlier works applying maximum likelihood estimation and related Cramer-Rao bounds [39, 69, 86, 87], and more emphasis on understanding the details of how cells can compute these estimates [88, 89] – which are not well understood for gradient sensing. In particular, earlier results on chemotaxis in elliptical cells [39] may potentially have similar discrepancies between MLE and Cramer-Rao. The Monte Carlo simulations within [39] do show agreement – but it is not clear whether this would hold in the more experimentally relevant regime where the difference between the circular variance and variance matters.

ACKNOWLEDGMENTS

We acknowledge support from NSF PHY 1915491 and NIH R35 GM142847. We thank Emiliano Perez Ipiña and Daiyue Sun for a close reading of the draft.

SUPPLEMENTARY INFORMATION: "CELL SHAPE AND ORIENTATION CONTROL GALVANOTACTIC ACCURACY"

Appendix A: Elliptic coordinates fundamentals

Elliptic coordinates are a standard orthogonal coordinate system that generalizes polar coordinates [46, 90–92]. In elliptic coordinates every point is determined by an elliptic radius μ and elliptic angle ν, analogous to the radius and polar angle in polar coordinates. A constant elliptic radius lies on the boundary of an ellipse, while a constant elliptic angle lies on a hyperbola that is horizontally oriented (Fig. S1). Ellipses and hyperbolae centered at the origin can be parameterized by $(R_1 \cos t, R_2 \sin t)$ and $(\alpha_1 \sec t, \alpha_2 \tan t)$, respectively. R_1, R_2 are the semi-major and minor axes of the ellipse. $2\alpha_1$ is the distance between the two vertices of the hyperbola. $\alpha_2^2 = a^2 - \alpha_1^2$, where a represents the focus point of the ellipses and hyperbolae, $a = \sqrt{R_1 - R_2}$. t is the variable of parameterization, where $t \in [0, 2\pi]$. The angle between the x-axis and the hyperbola asymptote is ν, which can be computed from the equation $\nu = \arctan\left[2\alpha_1\alpha_2/(\alpha_1^2 - \alpha_2^2)\right]$.

There are multiple conventions for representing Cartesian variables with elliptic variables. In this manuscript, we use the convention where $x = a\cosh\mu\cos\nu$ and $y = a\sinh\mu\sin\nu$. The unit vectors and scale factors are

$$\hat{\boldsymbol{\mu}} = \frac{a}{h_\mu}\begin{pmatrix}\sinh\mu\cos\nu\\ \cosh\mu\sin\nu\end{pmatrix}, \quad \hat{\boldsymbol{\nu}} = \frac{a}{h_\nu}\begin{pmatrix}-\cosh\mu\sin\nu\\ \sinh\mu\cos\nu\end{pmatrix}, \quad h_\mu = h_\nu = a\sqrt{\frac{\cosh 2\mu - \cos 2\nu}{2}}. \tag{A1}$$

Note h_μ and h_ν are equal. For our elliptical cell, placing the cell boundary at elliptical parameter $\mu = \mu_0$ means that the semi-major and semi-minor axes are $R_1 = a\cosh\mu_0$ and $R_2 = a\sinh\mu_0$. $\lambda = R_1/R_2$ is the aspect ratio.

To produce the field lines in Fig. 2 in the main text, it is sometimes easier to produce a grid in polar coordinates first, then to obtain expressions for both μ and ν in terms of the polar coordinates r and θ. There are established relationships we can use to map between Cartesian, polar, and elliptic coordinates, which we summarize here. We start with $x = r\cos\theta = a\cosh\mu\cos\nu$ and $y = r\sin\theta = a\sinh\mu\sin\nu$. Using Euler's formula and complex trigonometric relations $\cos\nu = \cosh i\nu$ and $i\sin\nu = \sinh i\nu$, we can derive a relationship between polar and elliptic coordinates.

$$\begin{aligned} re^{i\theta} &= r\left(\cos\theta + i\sin\theta\right) = a\left(\cosh\mu\cos\nu + i\sinh\mu\sin\nu\right)\\ &= a\left(\cosh\mu\cosh i\nu + \sinh\mu\sinh i\nu\right) = a\cosh\left(\mu + i\nu\right). \end{aligned} \tag{A2}$$

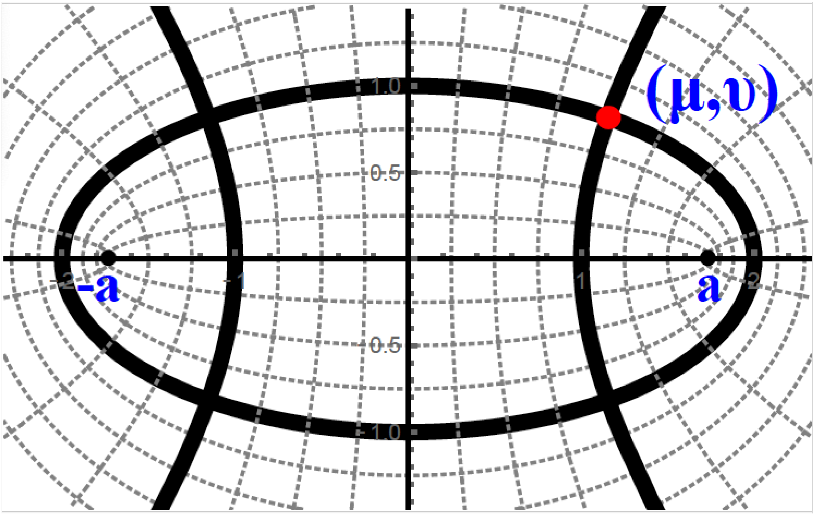

FIG. S1: Elliptic coordinate system displaying confocal ellipses and hyperbolae. Every point corresponds to the intersection of an ellipse (μ) and a hyperbola branch (ν). The foci for the ellipses and hyperbolae are at $\pm a$.

We now see that there is a straightforward relationship between (r, θ) and (μ, ν):

$$\mu(r,\theta) = \Re\left[\operatorname{arcosh}\left(\frac{r}{a}e^{i\theta}\right)\right], \tag{A3}$$

$$\nu(r,\theta) = \Im\left[\operatorname{arcosh}\left(\frac{r}{a}e^{i\theta}\right)\right], \tag{A4}$$

where $\Re(\cdot)$ and $\Im(\cdot)$ are the real and imaginary parts, respectively. The solutions are [93]

$$\mu = \operatorname{arcosh}\left(\frac{\mathfrak{A}_+ + \mathfrak{A}_-}{2a}\right), \tag{A5}$$

$$\nu = \frac{\sin\theta}{|\sin\theta|}\arccos\left(\frac{\mathfrak{A}_+ - \mathfrak{A}_-}{2a}\right), \tag{A6}$$

where $\mathfrak{A}_\pm = \sqrt{r^2 \pm 2ra\cdot\cos\theta + a^2}$. An equivalent result for ν has been derived [44]

$$\nu = \frac{\sin\theta}{|\sin\theta|}\arccos\left(\frac{r}{R_1}\cos\theta\right) = \frac{\sin\theta}{|\sin\theta|}\arccos\left(\frac{R_1R_2\cos\theta}{R_1\sqrt{(R_1\sin\theta)^2+(R_2\cos\theta)^2}}\right) = \frac{\sin\theta}{|\sin\theta|}\arccos\left(\frac{\cos\theta}{\sqrt{\lambda^2\sin^2\theta+\cos^2\theta}}\right), \tag{A7}$$

where $\lambda = R_1/R_2$ is defined as the ratio between the semi-major axis and the semi-minor axis lengths.

For completeness, we can also map from elliptic coordinates back to polar coordinates. We know that $r^2 = x^2 + y^2$ and $y/x = \tan\theta$. If we make use of the identities $\cos^2\nu + \sin^2\nu = 1$ and $\cosh^2\mu - \sinh^2\mu = 1$, we arrive at the identities [46]

$$r = a\sqrt{(\cosh^2\mu - \sin^2\nu)}, \tag{A8}$$

$$\theta = \arctan(\tanh\mu\tan\nu). \tag{A9}$$

Appendix B: Boundary conditions on the electric field

We assume a no-flux-like boundary condition, i.e. that there is no electric field normal to the membrane of the cell, $\mathbf{E}\cdot\hat{\mathbf{n}} = 0$. This boundary condition is physically motivated by the high resistivity (poor conductivity) of the cell membrane. The resistivity of the cell membrane is high (10^6–10^8 Ω·m) [44, 94–96] compared to the resistivity of the surrounding aqueous solution (∼0.008–0.8 Ω·m [96, 97]) and the cytoplasm (3 Ω·m [96]). Why does this lead to a no-flux boundary condition? One form of Gauss's law is

$$\nabla\cdot\mathbf{D} = \rho_f, \tag{B1}$$

where $\mathbf{D}$ is the displacement field and ρ_f is the free charge density. In linear media, $\mathbf{D} = \epsilon\mathbf{E}$. Using this relation and the definition $\mathbf{E} = -\nabla\Phi$, we can recast Gauss' law:

$$-\nabla\cdot(\epsilon\nabla\Phi) = \rho_f. \tag{B2}$$

Taking the time derivative on both sides and using the continuity equation $\partial_t\rho_f + \nabla\cdot\mathbf{J}_f = 0$, we can again rewrite Gauss' law:

$$-\nabla\cdot\left(\epsilon\nabla\frac{\partial\Phi}{\partial t}\right) = -\nabla\cdot\mathbf{J}_f, \tag{B3}$$

where $\mathbf{J}_f$ is the current density. At steady state, $\nabla\cdot\mathbf{J}_f = 0$. Ohm's law tells us that $\mathbf{J}_f = \sigma\mathbf{E} = -\sigma\nabla\Phi$. σ is the conductivity. This means that for Ohmic materials, the potential will obey [98]

$$0 = \nabla\cdot\left(\epsilon\nabla\frac{\partial\Phi}{\partial t}\right) + \nabla\cdot(\sigma\nabla\Phi). \tag{B4}$$

We assume that there is an effective steady state, the electric field is not changing rapidly, so we neglect the first term. Thus, the potential – inside the cell, outside the cell, or on the membrane – will obey

$$\nabla\cdot(\sigma\nabla\Phi) = 0. \tag{B5}$$

We can use this to establish the boundary conditions. To be in steady state, the current flux across a boundary must be continuous, so at the membrane-exterior fluid boundary, the field must obey

$$\mathbf{J}_f^{\text{membrane}}\cdot\hat{\mathbf{n}} = \mathbf{J}_f^{\text{fluid}}\cdot\hat{\mathbf{n}}, \tag{B6}$$

$$\sigma_{\text{membrane}}(\nabla\Phi)\cdot\hat{\mathbf{n}} = \sigma_{\text{fluid}}(\nabla\Phi)\cdot\hat{\mathbf{n}}, \tag{B7}$$

If the conductivity of the membrane can be neglected, $\sigma_{\text{membrane}} \approx 0$, then the boundary condition at the membrane surface reduces to simply $\nabla\Phi\cdot\hat{\mathbf{n}} = 0$.

Appendix C: Electric field around a circular cell

Before finding the electric field for the elliptical cell, doing so for a circular cell will provide some intuition. We solve Laplace's equation in cylindrical coordinates. We will assume that the potential is zero along the axial direction. Under this asumption, Laplace's equation takes the form:

$$\nabla^2\Phi = \frac{1}{r}\frac{\partial}{\partial r}\left(r\frac{\partial\Phi}{\partial r}\right) + \frac{1}{r^2}\frac{\partial^2\Phi}{\partial\theta^2} = 0. \tag{C1}$$

The most general form of the potential is [99]

$$\Phi(r,\theta) = a_0 + a_1\ln r + \sum_{k=1}^{\infty}\left(A_k r^k + B_k r^{-k}\right)\left(C_k\cos k\theta + D_k\sin k\theta\right). \tag{C2}$$

We can choose a reference point for our potential, so we can set $a_0 = 0$. Far away from the cell, we know that $\Phi = -E_0(x\cos\psi + y\sin\psi) \equiv -E_0 r(\cos\theta\cos\psi + \sin\theta\sin\psi) = -E_0 r\cos(\theta-\psi)$. This implies that the r^1 term is nonzero, while the remaining r^k terms go to zero. The r^{-k} terms are permitted, since we are only solving for the potential outside the cell, so the divergence at the origin is not a problem.

$$\Phi(r,\theta) = -E_0 r(\cos\theta\cos\psi + \sin\theta\sin\psi) + \sum_{k=1}^{\infty}\left(C_k\cos k\theta + D_k\sin k\theta\right)B_k r^{-k}, \tag{C3}$$

subject to the boundary condition $\partial_r\Phi = 0$ when $r = R_0$.

Applying the boundary condition to the potential on the outside of the cell gives us:

$$-E_0(\cos\theta\cos\psi + \sin\theta\sin\psi) - \sum_{k=1}^{\infty}k\left(C_k\cos k\theta + D_k\sin k\theta\right)B_k R_0^{-k-1} = 0. \tag{C4}$$

Matching the trigonometric terms order-by-order, all $k \neq 1$ terms are zero, and we find $-E_0 \cos\psi = C_1 B_1 R_0^{-2}$ and $-E_0 \sin\psi = D_1 B_1 R_0^{-2}$. We can then use this to rewrite the potential Φ as

$$\Phi(r, \theta) = -E_0 r \cos(\theta - \psi) - E_0 \frac{R_0^2}{r} \cos(\theta - \psi). \tag{C5}$$

The electric field can be found as $\mathbf{E} = -\nabla\Phi$:

$$\mathbf{E} = E_0 \left(1 - \frac{R_0^2}{r^2}\right) \cos(\theta - \psi)\hat{\mathbf{r}} - E_0 \left(1 + \frac{R_0^2}{r^2}\right) \sin(\theta - \psi)\hat{\boldsymbol{\theta}}. \tag{C6}$$

We see that, as we demanded, far from the cell the field is simply the applied electric field $\mathbf{E}_{\text{ext}} = E_0\hat{\mathbf{E}}$. However, close to the cell, the field deforms around the cell boundary – choosing $r = R_0$ we see that the field is completely tangential at the cell's surface, as required by our boundary condition. It is easy to see that the field tangent to the cell at the cell surface $r = R_0$ is

$$\mathbf{E}_{\|} = -2E_0 \sin(\theta - \psi)\hat{\boldsymbol{\theta}}. \tag{C7}$$

Appendix D: Electric field around an elliptical cell

We want to calculate the electric field along the boundary of the cell. To accomplish this, we solve for the tangential electric field in elliptical cylindrical coordinates. That first requires solving Laplace's equation $\nabla^2\Phi = 0$ in 2D. Laplace's equation in elliptical coordinates is:

$$\nabla^2\Phi = \frac{1}{h_\mu h_\nu} \left(\frac{\partial^2\Phi}{\partial\mu^2} + \frac{\partial^2\Phi}{\partial\nu^2}\right) = 0. \tag{D1}$$

$h_\mu = h_\nu$ are scale factors and $a = \sqrt{R_1^2 - R_2^2}$, assuming $R_1 > R_2$, where R_1 and R_2 are the lengths of the semi-major and minor axes, respectively. We can multiply both sides of Laplace's equation by $h_\mu h_\nu$ to simplify further. Let $\Phi(\mu, \nu) = M(\mu)N(\nu)$. By substituting and dividing through by Φ, we get:

$$\frac{1}{M}\frac{\partial^2 M}{\partial\mu^2} = -\frac{1}{N}\frac{\partial^2 N}{\partial\nu^2} = k^2. \tag{D2}$$

By inspection, solutions for N have the form $C_k e^{ik\nu}$. For M, we have to consider two cases. If $k = 0$, $M(\mu) = c_1\mu + c_0$. If $k \neq 0$, it is advantageous to guess a solution in the form $M(\mu) = c_{2k} \cosh k\mu + c_{3k} \sinh k\mu + c_{4k} e^{k\mu} + c_{5k} e^{-k\mu}$. This produces a general solution of the form

$$\Phi(\mu, \nu) = c_0 + c_1\mu + \sum_{k=1}^{\infty} C_k e^{ik\nu} [c_{2k} \cosh k\mu + c_{3k} \sinh k\mu + c_{4k} e^{k\mu} + c_{5k} e^{-k\mu}]. \tag{D3}$$

Just like for a circular cell, the cell is in a uniform applied field. We know that, far away from the cell ($\mu \to \infty$), the electric field potential outside should take the form $\Phi = -E_0(x\cos\psi + y\sin\psi) = -aE_0(\cosh\mu\cos\nu\cos\psi + \sinh\mu\sin\nu\sin\psi)$. This implies that our solution should take the form

$$\Phi = -aE_0(\cosh\mu\cos\nu\cos\psi + \sinh\mu\sin\nu\sin\psi) + \sum_{k=1}^{\infty} (\mathfrak{c}_k \cos k\nu + \mathfrak{d}_k \sin k\nu)\, e^{-k\mu}. \tag{D4}$$

Similar to the circle case, we have the boundary condition

$$\left.\frac{\partial\Phi}{\partial\mu}\right|_{\mu=\mu_0} = 0. \tag{D5}$$

We can see by matching trigonometric terms order-by-order that all terms with $k \neq 1$ are zero. The boundary condition then tells us that

$$-aE_0(\sinh\mu_0\cos\nu\cos\psi + \cosh\mu_0\sin\nu\sin\psi) = (\mathfrak{c}_1 \cos\nu + \mathfrak{d}_1 \sin\nu)\, e^{-\mu_0}. \tag{D6}$$

Collecting like terms for $\cos\nu$ and $\sin\nu$,

$$\mathfrak{c}_1 = -aE_0 e^{\mu_0}\sinh\mu_0\cos\psi, \tag{D7}$$

$$\mathfrak{d}_1 = -aE_0 e^{\mu_0}\cosh\mu_0\sin\psi. \tag{D8}$$

With substitution and some algebraic manipulations, the potential is expressed as:

$$\Phi = -E_0 a\left(\cosh\mu + \sinh\mu_0 e^{\mu_0-\mu}\right)\cos\nu\cos\psi - E_0 a\left(\sinh\mu + \cosh\mu_0 e^{\mu_0-\mu}\right)\sin\nu\sin\psi. \tag{D9}$$

(This is a well-known result; see Eq. 10.1.28 of [46].)

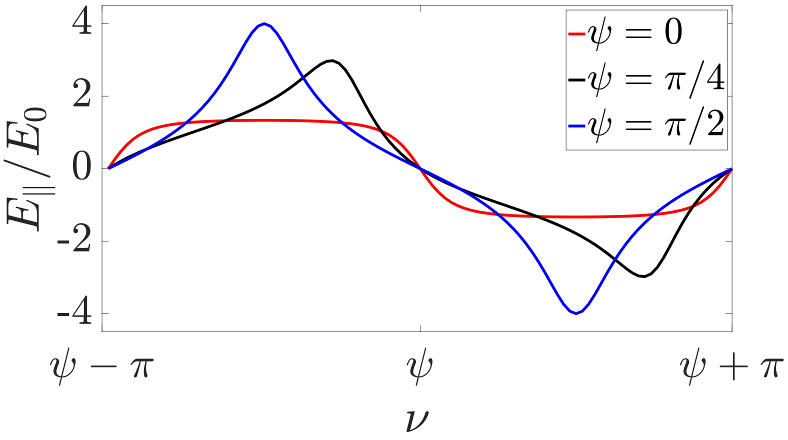

FIG. S2: Plot of magnitude of $\mathbf{E}_\parallel$ normalized by E_0. Discussed in the main text, this is proportional to the speed of sensors on the cell surface. A positive value means the tangential field is pointing along $+\hat{\boldsymbol{\nu}}$, which is defined in the counterclockwise direction.

The electric field outside the cell can be easily derived by taking the gradient in elliptic coordinates:

$$\mathbf{E} = -\nabla\Phi = -\frac{1}{h_\mu}\frac{\partial\Phi}{\partial\mu}\hat{\boldsymbol{\mu}} - \frac{1}{h_\nu}\frac{\partial\Phi}{\partial\nu}\hat{\boldsymbol{\nu}}. \tag{D10}$$

The outer field in its full form is

$$\mathbf{E} = \frac{E_0 a}{h_\mu}\frac{e^{\mu}-e^{2\mu_0-\mu}}{2}\cos(\nu-\psi)\hat{\boldsymbol{\mu}} - \frac{E_0 a}{h_\mu}\frac{e^{\mu}+e^{2\mu_0-\mu}}{2}\sin(\nu-\psi)\hat{\boldsymbol{\nu}}. \tag{D11}$$

It is easy to see that the field tangent to the cell at the cell surface $\mu=\mu_0$ is

$$\mathbf{E}_\parallel = -E_0\frac{ae^{\mu_0}}{h_{\mu_0}}\sin(\nu-\psi)\hat{\boldsymbol{\nu}}, \tag{D12}$$

where h_{μ_0} is h_μ evaluated at $\mu=\mu_0$. Fig. S2 plots Eq. (2) for different field directions ψ.

As a quick sanity check, does the result reduce to what we found for a circle? Note that for a circle, $a\to 0$ as $\mu_0\to\infty$. That manifests as $a\cosh\mu_0 = a\sinh\mu_0 = R_0$, $h_{\mu_0} = a\sqrt{(\cosh 2\mu_0 - \cos 2\nu)/2} = R_0$, and $ae^{\mu_0} = a(\cosh\mu_0+\sinh\mu_0) = 2R_0$. In this limit, the cell boundary is $x = R_0\cos\nu$ and $y = R_0\sin\nu$, so the elliptic angle ν is the same as the polar angle θ, and the tangential electric field is

$$\mathbf{E}_\parallel = -2E_0\sin(\theta-\psi)\hat{\boldsymbol{\theta}}. \tag{D13}$$

as we found above.

Appendix E: Probability distribution

We have derived the concentration of sensors $c(\nu) = c_0\exp\left[\kappa\cos(\nu-\psi)\right]$, the number of sensors per unit length of the membrane, in the main text. From this, we want to determine the probability density function for the elliptic

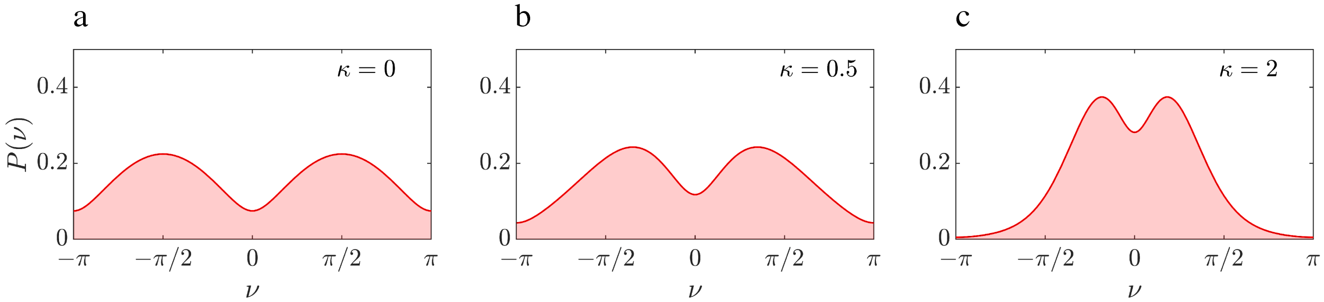

FIG. S3: Probability distributions at $\psi = 0$ as a function of the elliptic angle ν. The cell aspect ratio $\lambda = 3$. (a): $\mathcal{P}(\nu)$ for $\kappa = 0$. This is a uniform distribution on an ellipse. (b): $\mathcal{P}(\nu)$ for $\kappa = 0.5$. (c): $\mathcal{P}(\nu)$ for $\kappa = 2$.

angle ν of sensors. We know that the probability $\mathscr{P}(\nu)\mathrm{d}\nu$ to be in the region $\nu \cdots \nu + \mathrm{d}\nu$ is proportional to $c(\nu)\mathrm{d}l$ – where $\mathrm{d}l$ is the amount of arclength in this region. Changing variables, we expect

$$\mathscr{P}(\nu)\mathrm{d}\nu \sim c(\nu)\mathrm{d}l \tag{E1}$$

$$= c(\nu)\left|\frac{\mathrm{d}l}{\mathrm{d}\nu}\right|\mathrm{d}\nu \tag{E2}$$

$$= c(\nu)h_{\mu_0}\mathrm{d}\nu. \tag{E3}$$

We want our probability density to be normalized $\int_\gamma \mathscr{P}(\nu)\mathrm{d}\nu = 1$, where the integral is evaluated over the region $[\psi - \pi, \psi + \pi]$. We then get

$$\mathscr{P}(\nu) = Z^{-1}c(\nu)h_{\mu_0}, \tag{E4}$$

where

$$Z = \int_\gamma c(\nu)h_{\mu_0}\mathrm{d}\nu. \tag{E5}$$

Fig. S3 shows examples of this distribution for different values of κ. We note that even the limit of a uniform distribution ($\kappa = 0$) does not appear trivial – but this is only because of the complicated relationship between the perimeter of the cell and the elliptic angle ν. Taking this into account is essential to correctly sample sensor locations. If you, instead of sampling from Eq. (E4), attempted to generate uniformly distributed points by sampling ν uniformly over $[0, 2\pi]$, you would get an incorrect distribution of points (Fig. S4).

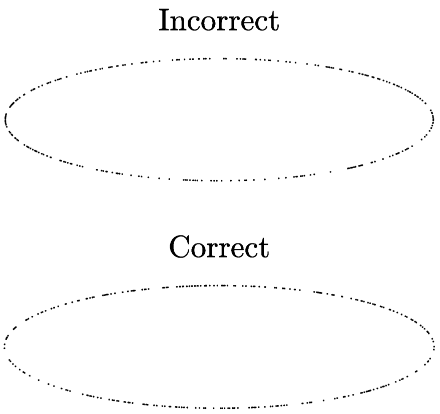

FIG. S4: Showing points sampled on ellipse. Incorrect sampling leads to higher density of points along high curvature regions.

Appendix F: Maximum likelihood and Fisher information

In the main text, we constructed the log likelihood function

$$\ln \mathcal{L} = \sum_{i=1}^{N} \left[\kappa \cos\left(\nu_i - \psi\right) + \ln h_{\mu_0}^{(i)}\right] - N \ln Z, \tag{F1}$$

and derived an expression for the estimator $\hat{\psi}$ by differentiating with respect to ψ. From here, we can also derive an expression for the Fisher information:

$$\mathcal{I} = \left\langle -\frac{\partial^2 \ln \mathcal{L}}{\partial \psi^2} \right\rangle = N \left[\frac{1}{Z}\frac{\partial^2 Z}{\partial \psi^2} - \left(\frac{1}{Z}\frac{\partial Z}{\partial \psi}\right)^2\right] + N\kappa \left\langle \cos\left(\nu - \psi\right)\right\rangle . \tag{F2}$$

We can easily compute from Eq. (7)

$$\left(\frac{1}{Z}\frac{\partial Z}{\partial \psi}\right)^2 = \kappa^2 \left\langle \sin\left(\nu - \psi\right)\right\rangle^2 . \tag{F3}$$

With some work, we can also see that

$$\frac{1}{Z}\frac{\partial^2 Z}{\partial \psi^2} = \kappa^2 \left\langle \sin^2 (\nu - \psi)\right\rangle - \kappa \left\langle \cos\left(\nu - \psi\right)\right\rangle . \tag{F4}$$

By combining the results and doing some algebra, we arrive at the Fisher information introduced in the main text:

$$\mathcal{I} = N\kappa^2 \left[\left\langle \sin^2\left(\nu - \psi\right)\right\rangle - \left\langle \sin\left(\nu - \psi\right)\right\rangle^2\right] . \tag{F5}$$

This result simplifies in the appropriate limits. For a circle, we know that $\left\langle \sin\left(\theta - \psi\right)\right\rangle = 0$ [30].

$$\mathcal{I} = N\kappa^2 \left\langle \sin^2\left(\theta - \psi\right)\right\rangle = \frac{N\kappa^2}{2\pi I_0(\kappa)} \int_{\gamma} \sin^2\left(\theta - \psi\right) \exp\left[\kappa \cos(\theta - \psi)\right] \mathrm{d}\theta. \;\; \text{(circle)} \tag{F6}$$

In this limit, the Fisher information becomes

$$\mathcal{I} = \frac{N\kappa}{I_0(\kappa)} \left[\frac{\kappa I_0(\kappa) - \kappa I_2(\kappa)}{2}\right] = N\kappa \frac{I_1(\kappa)}{I_0(\kappa)} \;\; \text{(circle)}, \tag{F7}$$

which is what we expect for a circle.

Appendix G: Perturbation calculations

To determine the maximum likelihood estimator for ψ and compute the Fisher information $\mathcal{I}$, we need to evaluate integrals for Z and $\partial Z/\partial \psi$, where $Z = \int_{\psi-\pi}^{\psi+\pi} c(\nu) h_{\mu_0} \mathrm{d}\nu$ as given in Eq. (7). These are then used in in Eqs. (10) and (12). We can evaluate these integrals numerically, and do so to compute the numerical bounds, but there is no general analytical solution. However, in this Appendix G, we derive simpler expressions for both the MLE and the Fisher information in certain relevant limits. In Appendix G 1, we assume that cells are nearly circular, simplifying the MLE in Eq. (10) and providing one simplified expression for the Fisher information in Eq. (12). In Appendix G 2, we derive two more simplified expressions for the Fisher information, one assuming that electric fields are weak, and another incorporating both assumptions, assuming that cells are nearly circular and that fields are weak simultaneously. In Appendix G 3, we summarize all the approximations for the Fisher information and explore some of their limiting behaviors.

1. Perturbation calculations for MLE and Fisher information for nearly circular cells

To derive a tractable analytical solution, we can assume that our cells are not too elongated. This approximation allows us to make a perturbation argument that simplifies the integrals and derive an expression for both the MLE in

Eq. (10) and the Fisher information in Eq. (12). The scale factor h_{μ_0} contains a square root that makes the integrals intractable. (Even integrating the scale factor by itself yields elliptic integrals!). Fortunately, it can be simplified greatly with a power series expansion. First, it is advantageous to rewrite the scale factor:

$$h_{\mu_0} = a\sqrt{\frac{\cosh 2\mu_0 - \cos 2\nu}{2}} = \sqrt{\frac{a^2\cosh 2\mu_0}{2}}\sqrt{1-\left(\frac{\cos 2\nu}{\cosh 2\mu_0}\right)}. \tag{G1}$$

If the cell is nearly circular, $\cosh 2\mu_0$ gets very large as μ_0 tends to infinity (required as $\lambda \to 1$), allowing us to Taylor expand the scale factor to first order in $(\cosh 2\mu_0)^{-1}$:

$$h_{\mu_0} \approx R_0\left[1-\frac{1}{2}\left(\frac{\cos 2\nu}{\cosh 2\mu_0}\right)-\cdots\right]. \tag{G2}$$

We will start by evaluating the partition function Z in the limit of a near-circular cell. We see

$$Z = \int_\gamma c(\nu) h_{\mu_0} \mathrm{d}\nu \tag{G3}$$

$$\approx R_0 \int_\gamma \exp\left[\kappa\cos(\nu-\psi)\right]\left[1-\frac{1}{2}\left(\frac{\cos 2\nu}{\cosh 2\mu_0}\right)\right]\mathrm{d}\nu. \tag{G4}$$

The integral over γ is a shorthand for the integral over the 2π range of ν, usually from $\psi-\pi$ to $\psi+\pi$. We also took the normalization factor $c_0 = 1$ without loss of generality – this will drop out of any probabilities. We can integrate this using some standard results for modified Bessel functions and using a substitution to $\alpha = \nu - \psi$, finding

$$Z \approx 2\pi R_0\left[I_0(\kappa) - \frac{1}{2}\frac{\cos 2\psi}{\cosh 2\mu_0} I_2(\kappa)\right] \tag{G5}$$

$$\equiv \chi(1-\epsilon), \tag{G6}$$

where $\chi = 2\pi R_0 I_0(\kappa)$ and $\epsilon = \cos 2\psi I_2(\kappa)[2I_0(\kappa)\cosh 2\mu_0]^{-1}$.

Similarly, we can evaluate the derivative $\frac{\partial Z}{\partial \psi}$, which is used in Eq. (10), using the approximation for h_{μ_0}:

$$\frac{\partial Z}{\partial \psi} \approx R_0\int_\gamma \kappa\sin(\nu-\psi)\exp\left[\kappa\cos(\nu-\psi)\right]\left[1-\frac{1}{2}\left(\frac{\cos 2\nu}{\cosh 2\mu_0}\right)\right]\mathrm{d}\nu. \tag{G7}$$

In this formula, the zeroth-order term in $(\cosh 2\mu_0)^{-1}$ will vanish because the integrand is odd. The next term can be evaluated similarly to the earlier integral,

$$\frac{\partial Z}{\partial \psi} \approx 2\pi R_0 \frac{\sin 2\psi}{\cosh 2\mu_0} I_2(\kappa). \tag{G8}$$

To finish the calculation of $\frac{1}{Z}\frac{\partial Z}{\partial \psi}$, which is on the right hand side of Eq. (10) for nearly circular cells, we expand Z^{-1} in the limit of nearly circular cells (which corresponds to small ϵ):

$$\frac{1}{Z} \approx \frac{1}{\chi(1-\epsilon)} \approx \frac{1}{\chi}\left(1+\epsilon+O(\epsilon^2)\right). \tag{G9}$$

Finally, we have

$$\frac{1}{Z}\frac{\partial Z}{\partial \psi} \approx \frac{1}{\chi}(1+\epsilon)\times 2\pi R_0\frac{\sin 2\psi}{\cosh 2\mu_0} I_2(\kappa) \tag{G10}$$

$$= \frac{\sin 2\hat{\psi}}{\cosh 2\mu_0}\frac{I_2(\kappa)}{I_0(\kappa)}(1+\epsilon) \tag{G11}$$

$$= \frac{\sin 2\hat{\psi}}{\cosh 2\mu_0}\frac{I_2(\kappa)}{I_0(\kappa)} + O(\epsilon^2), \tag{G12}$$

where in the last step we distribute the $(1+\epsilon)$ term and neglect all terms of order ϵ^2 since the prefactor $(\cosh 2\mu_0)^{-1} \sim \epsilon$, which is the small term we are expanding in.

Armed with this result for $\frac{1}{Z}\frac{\partial Z}{\partial \psi}$, we can find an approximate formula for the maximum likelihood estimator from Eq. (10),

$$\frac{1}{N}\sum_{i=1}^{N}\kappa\sin\left(\nu_i-\hat{\psi}\right)=\frac{\sin 2\hat{\psi}}{\cosh 2\mu_0}\frac{I_2(\kappa)}{I_0(\kappa)}. \tag{G13}$$

Using the identity $\sin(\nu-\hat{\psi})=\sin\nu\cos\hat{\psi}-\cos\nu\sin\hat{\psi}$, we can recast the equation as

$$\left(\frac{1}{N}\sum_{i=1}^{N}\sin\nu_i\right)\cos\hat{\psi}-\left(\frac{1}{N}\sum_{i=1}^{N}\cos\nu_i\right)\sin\hat{\psi}=\left[\frac{1}{\kappa\cosh 2\mu_0}\frac{I_2(\kappa)}{I_0(\kappa)}\right]\sin 2\hat{\psi}. \tag{G14}$$

The equation is in the form $A\cos\hat{\psi}-B\sin\hat{\psi}=C\sin 2\hat{\psi}$. We do not have an analytic solution to this, but we have solved this numerically and find consistent answers with our numerical optimization to find the maximum likelihood estimator.

More importantly, we can use this same perturbation technique to evaluate the integrals in Eq. (12) for the Fisher information. From Eq. (G14), we see that in the limit of large N, $N^{-1}\sum\sin\left(\nu-\psi\right)\to\langle\sin\left(\nu-\psi\right)\rangle\sim\left(\cosh 2\mu_0\right)^{-1}$. Since the Fisher information contains $\langle\sin\left(\nu-\psi\right)\rangle^2$, this term will be proportional to $\left(\cosh 2\mu_0\right)^{-2}$, which will be small in our Taylor expansion. Thus, we can ignore it and calculate the Fisher information in a more reduced form:

$$\mathcal{I}\approx N\kappa^2\left\langle\sin^2\left(\nu-\psi\right)\right\rangle. \tag{G15}$$

Expanding like we have done before:

$$\left\langle\sin^2\left(\nu-\psi\right)\right\rangle=\frac{1}{Z}\int_\gamma\sin^2\left(\nu-\psi\right)c(\nu)h_{\mu_0}\mathrm{d}\nu\approx(1+\epsilon)\frac{R_0}{\chi}\int_\gamma\sin^2\left(\nu-\psi\right)\exp\left[\kappa\cos(\nu-\psi)\right]\left[1-\frac{1}{2}\left(\frac{\cos 2\nu}{\cosh 2\mu_0}\right)\right]\mathrm{d}\nu. \tag{G16}$$

Using the substitution $\alpha=\nu-\psi$ again, the identity $\sin^2\alpha=(1-\cos 2\alpha)/2$, and common modified Bessel function relations, we can evaluate each of the two terms of the Taylor expansion in the integrand.

$$\begin{aligned}\left\langle\sin^2\left(\nu-\psi\right)\right\rangle&\approx\frac{R_0}{\chi}(1+\epsilon)\left[\frac{1}{2}\left[2\pi I_0(\kappa)-2\pi I_2(\kappa)\right]-\frac{2\pi I_2(\kappa)\cos 2\psi}{4\cosh 2\mu_0}+\frac{2\pi\cos 2\psi}{8\cosh 2\mu_0}\left[I_0(\kappa)+I_4(\kappa)\right]\right]\\&=\frac{1}{\kappa}\frac{I_1(\kappa)}{I_0(\kappa)}+\frac{\cos 2\psi}{8\kappa\cosh 2\mu_0}\left[4\frac{I_1(\kappa)I_2(\kappa)}{I_0^2(\kappa)}-\frac{\kappa[2I_2(\kappa)-I_0(\kappa)-I_4(\kappa)]}{4I_0(\kappa)}\right]+O(\epsilon^2).\end{aligned} \tag{G17}$$

We see now that, in the limit of nearly circular cells, the Fisher information reduces to

$$\mathcal{I}=N\kappa\frac{I_1(\kappa)}{I_0(\kappa)}+N\kappa\frac{\cos 2\psi}{8\cosh 2\mu_0}\left[\frac{4I_1(\kappa)I_2(\kappa)}{I_0^2(\kappa)}-\frac{\kappa[2I_2(\kappa)-I_0(\kappa)-I_4(\kappa)]}{I_0(\kappa)}\right]. \tag{G18}$$

The first term is exactly the Fisher information for a circle [30], while the second term is the first order correction. This can be rewritten

$$\mathcal{I}=N\kappa\left(\frac{I_1(\kappa)}{I_0(\kappa)}+\zeta_2\cos 2\psi\right), \tag{G19}$$

where

$$\zeta_2=\frac{1}{8\cosh 2\mu_0}\left[\frac{4I_1(\kappa)I_2(\kappa)}{I_0^2(\kappa)}-\frac{\kappa[2I_2(\kappa)-I_0(\kappa)-I_4(\kappa)]}{I_0(\kappa)}\right]. \tag{G20}$$

2. Small κ limit Fisher information

Experimentally, we suspect that the weak-field limit is most relevant. In our previous manuscript studying the physical limits of galvanotaxis on round cells [30], we discovered that the Fisher information for round cells simplifies to $N\kappa^2/d$, where $d=2,3$ for the dimension (circle versus sphere). Thus, it would nice to derive an expression for the Fisher information in this weak-field limit for an elliptical cell. This requires doing a Taylor expansion in κ. The concentration $c(\nu)$ is the only function that depends on κ and will be perturbed. We want the Fisher information to be of order κ^2 since it has a prefactor of κ^2. That would require us to expand the concentration to zeroth order in κ, meaning $c(\nu) \approx 1$. We noticed that at weak fields (small κ), $\partial_\psi Z \approx 0$, meaning that $\langle \sin(\nu - \psi) \rangle \approx 0$. We know this because

$$\frac{1}{Z}\frac{\partial Z}{\partial \psi} \approx \frac{\displaystyle\int_\gamma \kappa \sin(\nu - \psi)(1 + \cdots) h_{\mu_0} \mathrm{d}\nu}{\displaystyle\int_\gamma (1 + \cdots)\, h_{\mu_0} \mathrm{d}\nu}. \tag{G21}$$

where $\cdots$ indicates terms neglected in the limit of small κ. The numerator integrates to zero since

$$\int_\gamma \sin(\nu - \psi) h_{\mu_0} \mathrm{d}\nu = 0. \tag{G22}$$

This gives us Eq. (G15) again for the Fisher information:

$$\mathcal{I} \approx N\kappa^2 \left\langle \sin^2(\nu - \psi) \right\rangle. \tag{G23}$$

We only have to evaluate the average $\left\langle \sin^2(\nu - \psi) \right\rangle$ to zeroth order in κ – i.e. we evaluate it for a uniform distribution on the ellipse, or $c(\nu) = 1$. This gives us

$$\left\langle \sin^2(\nu - \psi) \right\rangle = \frac{1}{Z}\int_\gamma \sin^2(\nu - \psi) c(\nu) h_{\mu_0} \mathrm{d}\nu \approx \frac{\displaystyle\int_\gamma \sin^2(\nu - \psi) h_{\mu_0} \mathrm{d}\nu}{\displaystyle\int_\gamma h_{\mu_0} \mathrm{d}\nu}. \tag{G24}$$

Applying $\sin^2 x = (1 - \cos 2x)/2$:

$$\left\langle \sin^2(\nu - \psi) \right\rangle = \frac{1}{2} - \frac{1}{2\int_\gamma h_{\mu_0} \mathrm{d}\nu}\int_\gamma \cos[2(\nu - \psi)] h_{\mu_0} \mathrm{d}\nu \tag{G25}$$

$$\equiv \frac{1}{2} - (-\xi). \tag{G26}$$

Overall, we see that at small κ, the Fisher information takes the form

$$\mathcal{I} \approx N\kappa^2 \left(\frac{1}{2} + \xi\right), \tag{G27}$$

where

$$\xi = -\frac{1}{2\int_\gamma h_{\mu_0} \mathrm{d}\nu}\int_\gamma \cos[2(\nu - \psi)] h_{\mu_0} \mathrm{d}\nu. \tag{G28}$$

ξ is the anisotropic contribution, i.e. the contribution to the Fisher information from the eccentricity of the cell. The ψ dependence can be factored out of ξ. We must evaluate the integral to see this. The integral $\int \cos[2(\nu - \psi)] h_{\mu_0} \mathrm{d}\nu$ was evaluated in the interval $[0, 2\pi]$. This should be equivalent to integrating in the interval $[\psi - \pi, \psi + \pi]$. We see that

$$\begin{aligned}\int_\gamma \cos[2(\nu - \psi)] h_{\mu_0} \mathrm{d}\nu = {} & -\frac{a}{3}\cos 2\psi \left[(\cosh\mu_0 + \cosh 3\mu_0)\,\mathcal{E}\left(\frac{1}{\cosh^2\mu_0}\right) + 2\sinh\mu_0 \cosh 2\mu_0 \mathcal{E}\left(\frac{-1}{\sinh^2\mu_0}\right)\right] \\ & -\frac{a}{3}\cos 2\psi \left[-2\sinh\mu_0 \sinh 2\mu_0 \mathcal{K}\left(\frac{1}{\cosh^2\mu_0}\right) - 2\cosh\mu_0 \sinh 2\mu_0 \mathcal{K}\left(\frac{-1}{\sinh^2\mu_0}\right)\right],\end{aligned} \tag{G29}$$

where $\mathcal{K}(\cdot)$ and $\mathcal{E}(\cdot)$ are complete elliptical integrals of the first and second kinds, respectively, having the forms

$$\mathcal{K}(\Delta) = \int_0^{\pi/2} \mathrm{d}\nu \frac{1}{\sqrt{1 - \Delta \sin^2\nu}}, \qquad \mathcal{E}(\Delta) = \int_0^{\pi/2} \mathrm{d}\nu \sqrt{1 - \Delta \sin^2\nu}. \tag{G30}$$

We can also evaluate

$$Z(\kappa=0)=\int_\gamma h_{\mu_0}\mathrm{d}\nu=\int_\gamma a\sqrt{\frac{\cosh 2\mu_0-\cos 2\nu}{2}}\mathrm{d}\nu=2a\left[\mathcal{E}\left(\frac{1}{\cosh^2\mu_0}\right)\cosh\mu_0+\mathcal{E}\left(\frac{-1}{\sinh^2\mu_0}\right)\sinh\mu_0\right]. \tag{G31}$$

This normalization factor at zero field is simply the perimeter of the ellipse. We can see in Eq. (G29) that we can extract the ψ dependence:

$$\xi\equiv\zeta_1(\mu_0)\cos 2\psi. \tag{G32}$$

ζ_1 is another constant of aeolotropy, whose value is determined by the elliptical cell radius μ_0, which defines the cell surface. More anisotropic cells have smaller values for μ_0. Fully expanding, ζ_1 appears as

$$\zeta_1(\mu_0)=\frac{1}{12}\frac{(\cosh\mu_0+\cosh 3\mu_0)\,\mathcal{E}\left(\mathfrak{v}_1\right)+2\sinh\mu_0\cosh 2\mu_0\mathcal{E}\left(\mathfrak{v}_2\right)-2\sinh\mu_0\sinh 2\mu_0\mathcal{K}\left(\mathfrak{v}_1\right)-2\cosh\mu_0\sinh 2\mu_0\mathcal{K}\left(\mathfrak{v}_2\right)}{\cosh\mu_0\mathcal{E}\left(\mathfrak{v}_1\right)+\sinh\mu_0\mathcal{E}\left(\mathfrak{v}_2\right)}, \tag{G33}$$

where $\mathfrak{v}_1=1/\cosh^2\mu_0$ and $\mathfrak{v}_2=-1/\sinh^2\mu_0$. Now, we can express the Fisher information:

$$\mathcal{I}\approx N\kappa^2\left(\frac{1}{2}+\zeta_1\cos 2\psi\right). \tag{G34}$$

We derived Eq. (G34) from assuming the weak-field (small κ) limit and expanding Eq. (12) from the main text. We can also do a weak-field perturbation from Eq. (G18) which was derived solely for a nearly circular cell. Expanding each term so that the entire expression is of order κ^2, we see that

$$\mathcal{I}\approx N\kappa\left(\frac{\kappa}{2}+\cdots\right)+N\kappa\frac{\cos 2\psi}{8\cosh 2\mu_0}(\kappa+\cdots)=N\kappa^2\left(\frac{1}{2}+\zeta_0\cos 2\psi\right), \tag{G35}$$

where $\zeta_0(\mu_0)=(8\cosh 2\mu_0)^{-1}$ is the aeolotropic constant discussed in the main text.

3. Fisher information approximations and aeolotropic constants

We have been able to show that the Fisher information can be approximated in three different regimes: small κ, nearly circular cells, and both conditions combined. The approximations are

$$\mathcal{I}_0=N\kappa^2\left(\frac{1}{2}+\zeta_0\cos 2\psi\right)\quad\text{(small }\kappa\text{, near-circular)}, \tag{G36}$$

$$\mathcal{I}_1=N\kappa^2\left(\frac{1}{2}+\zeta_1\cos 2\psi\right)\quad\text{(small }\kappa\text{)}, \tag{G37}$$

$$\mathcal{I}_2=N\kappa\left(\frac{I_1(\kappa)}{I_0(\kappa)}+\zeta_2\cos 2\psi\right)\quad\text{(near-circular)}, \tag{G38}$$

where ζ_0, ζ_1, and ζ_2 are the aeolotropic constants.

$$\zeta_0=\frac{1}{8}\frac{1}{\cosh 2\mu_0}, \tag{G39}$$

$$\zeta_1=\frac{1}{12}\frac{(\cosh\mu_0+\cosh 3\mu_0)\,\mathcal{E}\left(\mathfrak{v}_1\right)+2\sinh\mu_0\cosh 2\mu_0\mathcal{E}\left(\mathfrak{v}_2\right)-2\sinh\mu_0\sinh 2\mu_0\mathcal{K}\left(\mathfrak{v}_1\right)-2\cosh\mu_0\sinh 2\mu_0\mathcal{K}\left(\mathfrak{v}_2\right)}{\cosh\mu_0\mathcal{E}\left(\mathfrak{v}_1\right)+\sinh\mu_0\mathcal{E}\left(\mathfrak{v}_2\right)}, \tag{G40}$$

$$\zeta_2=\frac{1}{8\cosh 2\mu_0}\left[\frac{4I_1(\kappa)I_2(\kappa)}{I_0^2(\kappa)}-\frac{\kappa[2I_2(\kappa)-I_0(\kappa)-I_4(\kappa)]}{I_0(\kappa)}\right]. \tag{G41}$$

ζ_0 and ζ_2 can easily be written in a more intuitive manner by representing them in terms of the aspect ratio λ. Recall that $\coth\mu_0=\lambda$. This means that

$$\cosh 2\mu_0=\cosh[2\text{arcoth}(\lambda)]=\frac{\lambda^2+1}{\lambda^2-1}. \tag{G42}$$

We can now rewrite the constants ζ_0 and ζ_2

$$\zeta_0 = \frac{1}{8}\frac{\lambda^2 - 1}{\lambda^2 + 1}, \tag{G43}$$

$$\zeta_2 = \zeta_0 \left[\frac{4I_1(\kappa)I_2(\kappa)}{I_0^2(\kappa)} - \frac{\kappa[2I_2(\kappa) - I_0(\kappa) - I_4(\kappa)]}{I_0(\kappa)}\right] \equiv \zeta_0 A(\kappa). \tag{G44}$$

The Fisher information consists of two components: the circular portion and the anisotropic portion. The circular portion represents the Fisher information for a circular cell. In contrast, the anisotropic portion accounts for the cell's eccentricity and is governed by aeolotropic constants. These aeolotropic constants should vanish when the Fisher information pertains to a circular cell. It is trivial to check that $\zeta_0 = \zeta_2 = 0$ when $\lambda = 1$. ζ_1 is less obvious. To see this, note that when we have a circle, all the elliptical integrals evaluate to $\pi/2$. This is because in the limit of a circle, $\lambda \to 1$ implies that $\mu_0 \to \infty$. Then, by multiplying ζ_1 by $1 = a/a$, the numerator of ζ_1 becomes

$$a\pi\left(\frac{1}{2}\cosh\mu_0 + \frac{1}{2}\cosh 3\mu_0 - \sinh\mu_0 \sinh 2\mu_0 - (\sinh 2\mu_0 \cosh\mu_0 - \sinh\mu_0 \cosh 2\mu_0)\right). \tag{G45}$$

We can use the identity $\sinh(x - y) = \sinh x \cosh y - \sinh y \cosh x$ to simplify the above expression

$$a\pi\left(\frac{1}{2}\cosh\mu_0 + \frac{1}{2}\cosh 3\mu_0 - \sinh\mu_0 \sinh 2\mu_0 - \sinh\mu_0\right). \tag{G46}$$

Similarly, we can use $\cosh(x \pm y) = \cosh x \cosh y \pm \sinh x \sinh y$ to simplify our expression in the numerator of ζ_1 further:

$$a\pi(\cosh\mu_0 - \sinh\mu_0) \equiv \pi(R_1 - R_2). \tag{G47}$$

Since $R_1 = R_2 = R_0$ for a circle, $\zeta_1 = 0$ and we have our desired limit.

We just showed that the aeolotropic constants have a minimum value $\zeta_{\min} = 0$ for a circle, which occurs when $\lambda = 1$. What are the values when we have an infinitely eccentric cell (1-dimensional line)? Do they have maxima? An infinitely eccentric cell occurs when $\mu_0 \to 0^+$ ($\lambda \to \infty$). In this limit, it is easy to see that $\zeta_0 \to 1/8$ and $\zeta_2 \to A(\kappa)/8$. Checking for ζ_1 is a bit tougher. We see that in this limit, $\cosh\mu_0 = 1$, $\sinh\mu_0 = 0$, $\mathcal{K}(\mathfrak{v}_2) = 0$, $\mathcal{E}(\mathfrak{v}_1) = 1$. $\mathcal{K}(\mathfrak{v}_1)$ becomes a complex number, where $\Re[\mathcal{K}(\mathfrak{v}_1)] \to \infty$ and $\Im[\mathcal{K}(\mathfrak{v}_1)] = \pi$. Meanwhile, $\mathcal{E}(\mathfrak{v}_2) \to \infty$. Fortunately, $\sinh\mu_0$ decreases at a faster rate than $\mathcal{K}(\cdot)$ and $\mathcal{E}(\cdot)$ can blow up. That means that $\zeta_1 \to (2 + 0 - 0 - 0)/12 = 1/6$. Armed with that information, we can summarize our findings:

$$\lim_{\mu_0 \to \infty} \zeta_0, \zeta_1, \zeta_2 \equiv \zeta_{\min} = 0 \quad \text{(circle)}, \tag{G48}$$

$$\lim_{\mu_0 \to 0^+} \zeta_0 = \frac{1}{8}, \quad \lim_{\mu_0 \to 0^+} \zeta_1 = \frac{1}{6}, \quad \lim_{\mu_0 \to 0^+} \zeta_2 = \frac{A(\kappa)}{8} \quad \text{(line)}. \tag{G49}$$

Appendix H: Normal approximation and fitting γ

In the main text, we claim that the directionality, the measure of how well cells follow electric fields [30, 100], is $\langle\cos(\hat{\psi} - \psi)\rangle \approx e^{-\mathcal{I}^{-1}/2}$. This is an alternate formula to $\langle\cos(\hat{\psi} - \psi)\rangle \approx \sqrt{\mathcal{I}/(1 + \mathcal{I})}$, which we used in [30]. We show fits to both forms in Fig. S5. This alternate directionality formula was derived by taking advantage of the property that maximum likelihood estimators are asymptotically normal in the limit of large sample sizes [101, 102]. Thus, for a sufficiently large sample of sensors N, even the periodic estimator $\hat{\psi} \xrightarrow{\text{d}} \mathcal{N}(\psi, \mathcal{I}^{-1})$. (Note that in the literature, the Fisher information per observation $\mathcal{I}_N$ is often used, making the limiting variance $(N\mathcal{I}_N)^{-1} = \mathcal{I}^{-1}$). That means the density for $\hat{\psi}$ can be approximated by a Gaussian distribution

$$f(\hat{\psi}) \approx \sqrt{\frac{\mathcal{I}}{2\pi}} \exp\left[-\frac{\mathcal{I}}{2}(\hat{\psi} - \psi)^2\right]. \tag{H1}$$

With this probability density function, $\langle\cos(\hat{\psi} - \psi)\rangle$ can be computed

$$\langle\cos(\hat{\psi} - \psi)\rangle \approx \int_{-\infty}^{\infty} \cos(\hat{\psi} - \psi) f(\hat{\psi}) \mathrm{d}\hat{\psi} = e^{-\mathcal{I}^{-1}/2}. \tag{H2}$$

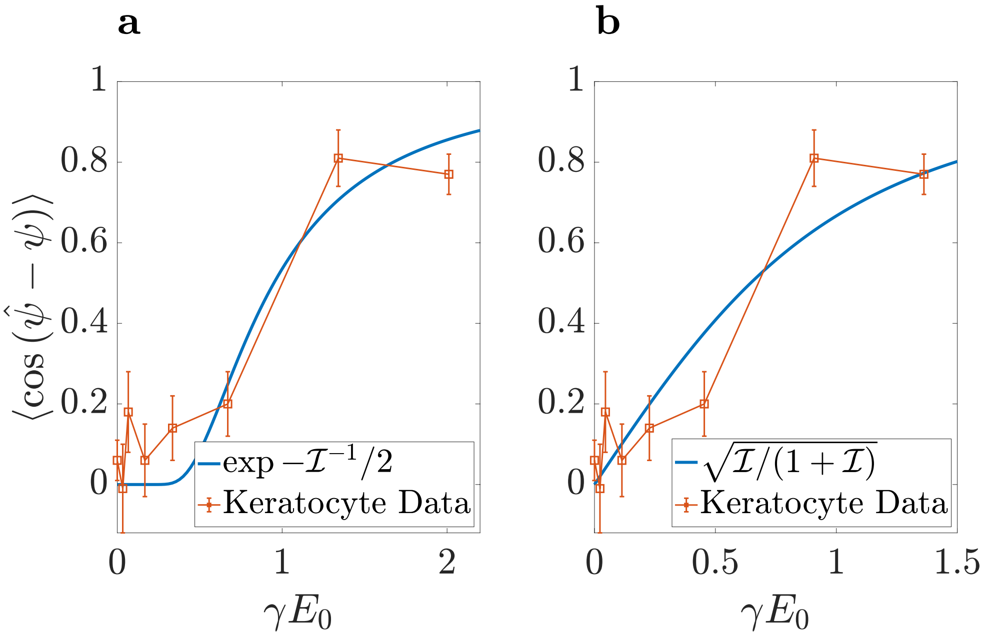

FIG. S5: Plots fitting Eq. (H2) directionality to keratocyte data where $\mathcal{I} = 0.8(\gamma E_0)^2$. (a) Fit with $e^{\mathcal{I}^{-1}/2}$, yielding a fit value of $\gamma = 3.4 \times 10^{-3}$ mm/mV. (b) Fit with $\sqrt{\mathcal{I}/(\mathcal{I}+1)}$, yielding a fit value of $\gamma = 2.3 \times 10^{-3}$ mm/mV.

We derive the Fisher information limit appropriate for keratocytes in Eq. (16) in the main text. We use this result to fit the directionality $\langle \cos(\hat{\psi}-\psi) \rangle$ to keratocyte experimental data from [57] to determine a reasonable value for γ, the characteristic electric field strength. Data of keratocyte directionality as a function of field strength was fitted using Eq. (16) and plugging it into Eq. (H2). This fitting process produced $\gamma = 3.4 \times 10^{-3}$ mm/mV (Fig. S5a). We see in Fig. S5 that the normal-approximation assumption is a slightly better fit to the experimental data, though we are not confident that this data can really discriminate between the two models. The difference in γ in fitting to these two models is relatively small. However, there would be minor quantitative changes if we chose the alternate value of $\gamma = 2.3 \times 10^{-3}$ mm/mV. This sets the scale of electric field the cell can sense, and would make the transition in trends in Fig. 5 in the main text occur at a higher field strength and the magnitude of the variance decrease more slowly as the electric field strength is increased.

Appendix I: Circular variance derived from MLE for keratocytes as a function of sensor number N

We found that the Fisher information does not depend on β and N independently, but only on the combination $\gamma = N\beta^2/2$. However, because in the limit of weak fields, the maximum likelihood estimator's variance is above the Cramer-Rao bound, it is possible that the MLE variance depends separately on N and β. Here, we show how the circular variance changes while the number of sensors N changes, while keeping γ constant – and thus keeping the magnitude of the Fisher information constant. If we fix $\gamma = 3.4 \times 10^{-3}$ mm/mV, then the behavior of the circular variance is unaffected by changing N (Fig. S6). According to the simulations, the circular variance remains maximal when the electric field is parallel to the cell's long axis and minimal if the field is parallel to the cell's short axis.

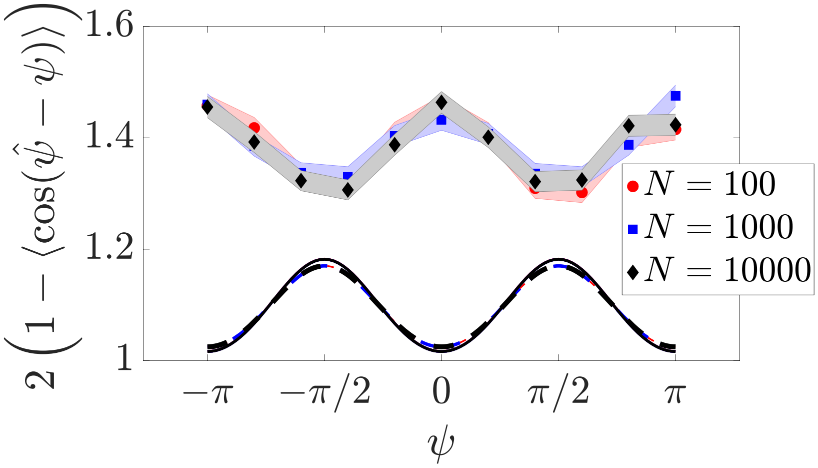

FIG. S6: Circular variance plots for keratocytes calculated using MLE. $\gamma = 3.4 \times 10^{-3}$ mm/mV is kept constant. Simulated for 5000 cells at a field strength $E_0 = 150$ mV/mm. Varied for $N = 100$ ($\kappa \approx 5 \times 10^{-2}$), $N = 1000$ ($\kappa \approx 1.5 \times 10^{-2}$), and $N = 10000$ ($\kappa \approx 5 \times 10^{-3}$). Solid lines is the lower bound from Eq. (13). Dashed lines are the lower bound from Eq. (14). Shaded region are error bars for standard error of the mean.

REFERENCES

---

[1] Luigi Galvani, Giovanni Aldini, et al. *De viribus electricitatis in motu musculari: commentarius cum Joannis Aldini dissertatione et notis: accesserunt epistolae ad animalis electricitatis theoriam pertinentes.* Soc. Typogr., 1792.

[2] Luigi Galvani and Duane HD Roller. Commentary on the effect of electricity on muscular motion. *American Journal of Physics*, 22(1):40–40, 1954.

[3] Colin D McCaig, Ann M Rajnicek, Bing Song, and Min Zhao. Controlling cell behavior electrically: current views and future potential. *Physiological reviews*, 2005.

[4] Riyi Shi and Richard B Borgens. Three-dimensional gradients of voltage during development of the nervous system as invisible coordinates for the establishment of embryonic pattern. *Developmental Dynamics*, 202(2):101–114, 1995.

[5] Kevin B Hotary and Kenneth R Robinson. Endogenous electrical currents and voltage gradients in xenopus embryos and the consequences of their disruption. *Developmental biology*, 166(2):789–800, 1994.

[6] ME Mourey Metcalf and Richard B Borgens. Weak applied voltages interfere with amphibian morphogenesis and pattern. *Journal of Experimental Zoology*, 268(4):323–338, 1994.

[7] Kevin B Hotary and Kenneth R Robinson. Evidence of a role for endogenous electrical fields in chick embryo development. *Development*, 114(4):985–996, 1992.

[8] Christine E Pullar and R Rivkah Isseroff. Cyclic amp mediates keratinocyte directional migration in an electric field. *Journal of cell science*, 118(9):2023–2034, 2005.

[9] Richard Nuccitelli. Endogenous electric fields in embryos during development, regeneration and wound healing. *Radiation protection dosimetry*, 106(4):375–383, 2003.

[10] Richard Nuccitelli. A role for endogenous electric fields in wound healing. *Current topics in developmental biology*, 58(2):1–26, 2003.

[11] Richard HW Funk. Endogenous electric fields as guiding cue for cell migration. *Frontiers in physiology*, 6:143, 2015.

[12] Xi Ren, Huanbo Sun, Jie Liu, Xiaowei Guo, Jingzhuo Huang, Xupin Jiang, Yiming Zhang, Yuesheng Huang, Dongli Fan, and Jiaping Zhang. Keratinocyte electrotaxis induced by physiological pulsed direct current electric fields. *Bioelectrochemistry*, 127:113–124, 2019.

[13] Yi Liang, Hao Tian, Jie Liu, YanLing Lv, Yuan Wang, JiaPing Zhang, and YueSheng Huang. Application of stable continuous external electric field promotes wound healing in pig wound model. *Bioelectrochemistry*, 135:107578, 2020.

[14] Yunita Sari, Eman Sutrisna, et al. The effect of short duration of electrical stimulation on wound healing in acute wound in a rat model. *Wound Medicine*, 24(1):36–44, 2019.

[15] Menglu Li, Xiaofeng Wang, Pandey Rajagopalan, Liang Zhang, Shijie Zhan, Shuyi Huang, Wei Li, Xiangyu Zeng, Qikai Ye, Yulu Liu, et al. Toward controlled electrical stimulation for wound healing based on a precision layered skin model. *ACS Applied Bio Materials*, 3(12):8901–8910, 2020.

[16] Greg M Allen, Alex Mogilner, and Julie A Theriot. Electrophoresis of cellular membrane components creates the directional cue guiding keratocyte galvanotaxis. *Current Biology*, 23(7):560–568, 2013.

[17] Brian M Kobylkevich, Anyesha Sarkar, Brady R Carlberg, Ling Huang, Suman Ranjit, David M Graham, and Mark A Messerli. Reversing the direction of galvanotaxis with controlled increases in boundary layer viscosity. *Physical Biology*, 15(3):036005, 2018.

[18] Kan Zhu, Yaohui Sun, Anh Miu, Michael Yen, Bowei Liu, Qunli Zeng, Alex Mogilner, and Min Zhao. camp and cgmp play an essential role in galvanotaxis of cell fragments. *Journal of cellular physiology*, 231(6):1291–1300, 2016.

[19] Francis X Hart, Mhairi Laird, Aimie Riding, and Christine E Pullar. Keratinocyte galvanotaxis in combined dc and ac electric fields supports an electromechanical transduction sensing mechanism. *Bioelectromagnetics*, 34(2):85–94, 2013.

[20] Donna R Trollinger, R Rivkah Isseroff, and Richard Nuccitelli. Calcium channel blockers inhibit galvanotaxis in human keratinocytes. *Journal of cellular physiology*, 193(1):1–9, 2002.

[21] Hans Gruler and Kurt Franke. Automatic control and directed cell movement novel approach for understanding chemotaxis, galvanotaxis, galvanotropism. *Zeitschrift für Naturforschung C*, 45(11-12):1241–1249, 1990.

[22] Hans Gruler and Richard Nuccitelli. Neural crest cell galvanotaxis: new data and a novel approach to the analysis of both galvanotaxis and chemotaxis. *Cell motility and the cytoskeleton*, 19(2):121–133, 1991.

[23] K Franke and H Gruler. Galvanotaxis of human granulocytes: electric field jump studies. *European Biophysics Journal*, 18:334–346, 1990.

[24] Hans Gruler and Richard Nuccitelli. New insights into galvanotaxis and other directed cell movements: an analysis of the translocation distribution function. *Progress in Clinical and Biological Research*, 210:337–347, 1986.

[25] Carol A Erickson and Richard Nuccitelli. Embryonic fibroblast motility and orientation can be influenced by physiological electric fields. *The Journal of cell biology*, 98(1):296–307, 1984.

[26] Martin J Brown and Leslie M Loew. Electric field-directed fibroblast locomotion involves cell surface molecular reorganization and is calcium independent. *The Journal of cell biology*, 127(1):117–128, 1994.

[27] Richard Nuccitelli and Tanya Smart. Extracellular calcium levels strongly influence neural crest cell galvanotaxis. *The Biological Bulletin*, 176(2S):130–135, 1989.

[28] Richard Nuccitelli, Tanya Smart, and James Ferguson. Protein kinases are required for embryonic neural crest cell galvanotaxis. *Cell motility and the cytoskeleton*, 24(1):54–66, 1993.

[29] St McLaughlin and MM Poo. The role of electro-osmosis in the electric-field-induced movement of charged macromolecules on the surfaces of cells. *Biophysical journal*, 34(1):85–93, 1981.

[30] Ifunanya Nwogbaga, A Hyun Kim, and Brian A Camley. Physical limits on galvanotaxis. *Physical Review E*, 108(6):064411, 2023.

[31] Anyesha Sarkar, Brian M Kobylkevich, David M Graham, and Mark A Messerli. Electromigration of cell surface macromolecules in dc electric fields during cell polarization and galvanotaxis. *Journal of theoretical biology*, 478:58–73, 2019.

[32] Aimie Riding and Christine E Pullar. Atp release and p2y receptor signaling are essential for keratinocyte galvanotaxis. *Journal of cellular physiology*, 231(1):181–191, 2016.

[33] Kathy S Fang, Edward Ionides, George Oster, Richard Nuccitelli, and R Rivkah Isseroff. Epidermal growth factor receptor relocalization and kinase activity are necessary for directional migration of keratinocytes in dc electric fields. *Journal of cell science*, 112(12):1967–1978, 1999.

[34] Ling Huang, Peter Cormie, Mark A Messerli, and Kenneth R Robinson. The involvement of ca2+ and integrins in directional responses of zebrafish keratocytes to electric fields. *Journal of cellular physiology*, 219(1):162–172, 2009.

[35] Christine E Pullar, Brian S Baier, Yoshinobu Kariya, Alan J Russell, Basil AJ Horst, M Peter Marinkovich, and R Rivkah Isseroff. $\beta 4$ integrin and epidermal growth factor coordinately regulate electric field-mediated directional migration via rac1. *Molecular biology of the cell*, 17(11):4925–4935, 2006.

[36] Bo-jian Lin, Shun-hao Tsao, Alex Chen, Shu-Kai Hu, Ling Chao, and Pen-hsiu Grace Chao. Lipid rafts sense and direct electric field-induced migration. *Proceedings of the National Academy of Sciences*, 114(32):8568–8573, 2017.

[37] Hsin-ya Yang, Roch-Philippe Charles, Edith Hummler, Deborah L Baines, and R Rivkah Isseroff. The epithelial sodium channel mediates the directionality of galvanotaxis in human keratinocytes. *Journal of cell science*, 126(9):1942–1951, 2013.

[38] Slawomir Lasota, Eliza Zimolag, Sylwia Bobis-Wozowicz, Jagoda Pilipiuk, and Zbigniew Madeja. The dynamics of the electrotactic reaction of mouse 3t3 fibroblasts. *Biochimica et Biophysica Acta (BBA)-Molecular Cell Research*, 1871(2):119647, 2024.

[39] Bo Hu, Wen Chen, Wouter-Jan Rappel, and Herbert Levine. How geometry and internal bias affect the accuracy of eukaryotic gradient sensing. *Physical Review E*, 83(2):021917, 2011.

[40] Juliet Lee, Akira Ishihara, Julie A Theriot, and Ken Jacobson. Principles of locomotion for simple-shaped cells. *Nature*, 362(6416):167–171, 1993.

[41] Brian A Camley, Yanxiang Zhao, Bo Li, Herbert Levine, and Wouter-Jan Rappel. Crawling and turning in a minimal reaction-diffusion cell motility model: Coupling cell shape and biochemistry. *Physical Review E*, 95(1):012401, 2017.

[42] Takao Ohta, Takahiro Ohkuma, and Kyohei Shitara. Deformation of a self-propelled domain in an excitable reaction-diffusion system. *Physical Review E*, 80(5):056203, 2009.

[43] Gawoon Shim, Danelle Devenport, and Daniel J Cohen. Overriding native cell coordination enhances external programming of collective cell migration. *Proceedings of the National Academy of Sciences*, 118(29), 2021.

[44] Tadej Kotnik and Damijan Miklavčič. Analytical description of transmembrane voltage induced by electric fields on spheroidal cells. *Biophysical Journal*, 79(2):670–679, 2000.

[45] Brian J Mossop, Roger C Barr, David A Zaharoff, and Fan Yuan. Electric fields within cells as a function of membrane resistivity-a model study. *IEEE transactions on nanobioscience*, 3(3):225–231, 2004.

[46] Philip M Morse and Herman Feshbach. Methods of theoretical physics. *American Journal of Physics*, 22(6):410–413, 1954.

[47] Parry Moon and Domina E Spencer. *Field theory handbook: including coordinate systems, differential equations and their solutions*. Springer, 2012.

[48] J Th G Overbeek and Ph H Wiersema. The interpretation of electrophoretic mobilities. In *Electrophoresis*, pages 1–52. Elsevier, 1967.

[49] KV Mardia and PJ Zemroch. Algorithm as 86: The von mises distribution function. *Journal of the Royal Statistical Society. Series C (Applied Statistics)*, 24(2):268–272, 1975.

[50] L Gary Leal. *Advanced transport phenomena: fluid mechanics and convective transport processes*, volume 7. Cambridge University Press, 2007.

[51] George Casella, Christian P Robert, and Martin T Wells. Generalized accept-reject sampling schemes. *Lecture Notes-Monograph Series*, pages 342–347, 2004.

[52] Jeffrey C Lagarias, James A Reeds, Margaret H Wright, and Paul E Wright. Convergence properties of the nelder–mead simplex method in low dimensions. *SIAM Journal on optimization*, 9(1):112–147, 1998.

[53] Kinneret Keren, Zachary Pincus, Greg M Allen, Erin L Barnhart, Gerard Marriott, Alex Mogilner, and Julie A Theriot. Mechanism of shape determination in motile cells. *Nature*, 453(7194):475–480, 2008.

[54] Steven M Kay. *Fundamentals of statistical signal processing: estimation theory*. Prentice-Hall, Inc., 1993.

[55] Greg M Allen, Kun Chun Lee, Erin L Barnhart, Mark A Tsuchida, Cyrus A Wilson, Edgar Gutierrez, Alexander Groisman, Julie A Theriot, and Alex Mogilner. Cell mechanics at the rear act to steer the direction of cell migration. *Cell Systems*, 11(3):286–299, 2020.

[56] JULIET Lee, AK1RA Ishihara, and K Jacobson. The fish epidermal keratocyte as a model system for the study of cell locomotion. In *Symposia of the Society for Experimental Biology*, volume 47, pages 73–89, 1993.

[57] Yaohui Sun, Hao Do, Jing Gao, Ren Zhao, Min Zhao, and Alex Mogilner. Keratocyte fragments and cells utilize competing pathways to move in opposite directions in an electric field. *Current Biology*, 23(7):569–574, 2013.

[58] Tatsat Banerjee, Debojyoti Biswas, Dhiman Sankar Pal, Yuchuan Miao, Pablo A Iglesias, and Peter N Devreotes. Spatiotemporal dynamics of membrane surface charge regulates cell polarity and migration. *Nature cell biology*, 24(10):1499–1515, 2022.

[59] Kanti V Mardia, Peter E Jupp, and KV Mardia. *Directional statistics*, volume 2. Wiley Online Library, 2000.

[60] Kurmanbek Kaiyrbekov and Brian A Camley. Does nematic order allow groups of elongated cells to sense electric fields better? *arXiv preprint arXiv:2404.04723*, 2024.

[61] Paul W Luther, H Benjamin Peng, and Jim Jung-Ching Lin. Changes in cell shape and actin distribution induced by constant electric fields. *Nature*, 303(5912):61–64, 1983.

[62] Edward K Onuma and Sek-Wen Hui. Electric field-directed cell shape changes, displacement, and cytoskeletal reorganization are calcium dependent. *The Journal of cell biology*, 106(6):2067–2075, 1988.

[63] Takao Ohta and Takahiro Ohkuma. Deformable Self-Propelled Particles. *Physical Review Letters*, 102(15):154101, 2009.

[64] T Hiraiwa, MY Matsuo, T Ohkuma, T Ohta, and M Sano. Dynamics of a deformable self-propelled domain. *Europhysics Letters*, 91(2):20001, 2010.

[65] Danying Shao, Wouter-Jan Rappel, and Herbert Levine. Computational model for cell morphodynamics. *Physical review letters*, 105(10):108104, 2010.

[66] Brian A Camley, Yunsong Zhang, Yanxiang Zhao, Bo Li, Eshel Ben-Jacob, Herbert Levine, and Wouter-Jan Rappel. Polarity mechanisms such as contact inhibition of locomotion regulate persistent rotational motion of mammalian cells on micropatterns. *Proceedings of the National Academy of Sciences*, 111(41):14770–14775, 2014.

[67] T Ohta, M Mimura, and Ryo Kobayashi. Higher-dimensional localized patterns in excitable media. *Physica D: Nonlinear Phenomena*, 34(1-2):115–144, 1989.

[68] Charles W Wolgemuth, Jelena Stajic, and Alex Mogilner. Redundant mechanisms for stable cell locomotion revealed by minimal models. *Biophysical journal*, 101(3):545–553, 2011.

[69] Emiliano Perez Ipiña and Brian A Camley. Collective gradient sensing with limited positional information. *Physical Review E*, 105(4):044410, 2022.

[70] Sean Fancher and Andrew Mugler. Fundamental limits to collective concentration sensing in cell populations. *Physical review letters*, 118(7):078101, 2017.

[71] William Bialek and Sima Setayeshgar. Physical limits to biochemical signaling. *Proceedings of the National Academy of Sciences*, 102(29):10040–10045, 2005.

[72] Pieter Rein ten Wolde, Nils B Becker, Thomas E Ouldridge, and Andrew Mugler. Fundamental limits to cellular sensing. *Journal of Statistical Physics*, 162:1395–1424, 2016.

[73] Brian A Camley. Collective gradient sensing and chemotaxis: modeling and recent developments. *Journal of Physics: Condensed Matter*, 30(22):223001, 2018.

[74] Luke Tweedy, Börn Meier, Jürgen Stephan, Doris Heinrich, and Robert G Endres. Distinct cell shapes determine accurate chemotaxis. *Scientific reports*, 3(1):2606, 2013.

[75] Kento Nakamura and Tetsuya J Kobayashi. Gradient sensing limit of a cell when controlling the elongating direction. *arXiv preprint arXiv:2405.04810*, 2024.

[76] Abijeet Singh Mehta, Pin Ha, Kan Zhu, ShiYu Li, Kang Ting, Chia Soo, Xinli Zhang, and Min Zhao. Physiological electric fields induce directional migration of mammalian cranial neural crest cells. *Developmental biology*, 471:97–105, 2021.

[77] Liang Guo, Chunyan Xu, Dong Li, Xiulan Zheng, Jiebing Tang, Jingyi Bu, Hui Sun, Zhengkai Yang, Wenjing Sun, and Xiaoguang Yu. Calcium ion flow permeates cells through socs to promote cathode-directed galvanotaxis. *PloS one*, 10(10):e0139865, 2015.

[78] Huai Bai, Colin D McCaig, John V Forrester, and Min Zhao. Dc electric fields induce distinct preangiogenic responses in microvascular and macrovascular cells. *Arteriosclerosis, thrombosis, and vascular biology*, 24(7):1234–1239, 2004.

[79] Zhiqiang Zhao, Lu Qin, Brian Reid, Jin Pu, Takahiko Hara, and Min Zhao. Directing migration of endothelial progenitor cells with applied dc electric fields. *Stem cell research*, 8(1):38–48, 2012.

[80] Spencer J Bunn, Alexander Lai, and Jianming Li. Dc electric fields induce perpendicular alignment and enhanced migration in schwann cell cultures. *Annals of biomedical engineering*, 47:1584–1595, 2019.

[81] MS Cooper and RE Keller. Perpendicular orientation and directional migration of amphibian neural crest cells in dc electrical fields. *Proceedings of the National Academy of Sciences*, 81(1):160–164, 1984.

[82] AM Rajnicek, NA Gow, and CD McCaig. Electric field-induced orientation of rat hippocampal neurones in vitro. *Experimental Physiology: Translation and Integration*, 77(1):229–232, 1992.

[83] Nina Tandon, Brian Goh, Anna Marsano, Pen-Hsiu Grace Chao, Chrystina Montouri-Sorrentino, Jeffrey Gimble, and Gordana Vunjak-Novakovic. Alignment and elongation of human adipose-derived stem cells in response to direct-current electrical stimulation. In *2009 annual international conference of the IEEE engineering in medicine and biology society*, pages 6517–6521. IEEE, 2009.

[84] Masayuki J Sato, Michihito Ueda, Hiroaki Takagi, Tomonobu M Watanabe, Toshio Yanagida, and Masahiro Ueda. Input–output relationship in galvanotactic response of dictyostelium cells. *Biosystems*, 88(3):261–272, 2007.

[85] Mary Lang, Spencer Bunn, Bhavani Gopalakrishnan, and Jianming Li. Use of weak dc electric fields to rapidly align mammalian cells. *Journal of Neural Engineering*, 18(5):054002, 2021.

[86] Robert G Endres and Ned S Wingreen. Maximum likelihood and the single receptor. *Physical review letters*, 103(15):158101, 2009.

[87] Austin Hopkins and Brian A Camley. Chemotaxis in uncertain environments: Hedging bets with multiple receptor types. *Physical Review Research*, 2(4):043146, 2020.

[88] Pankaj Mehta and David J Schwab. Energetic costs of cellular computation. *Proceedings of the National Academy of Sciences*, 109(44):17978–17982, 2012.

[89] Vijay Singh and Ilya Nemenman. Simple biochemical networks allow accurate sensing of multiple ligands with a single receptor. *PLoS Computational Biology*, 13(4):e1005490, 2017.

[90] Ernest William Hobson. *The theory of spherical and ellipsoidal harmonics.* CUP Archive, 1931.

[91] Granino Arthur Korn and Theresa M Korn. *Mathematical handbook for scientists and engineers: definitions, theorems, and formulas for reference and review.* Courier Corporation, 2000.

[92] Gaston Darboux. *Leçons sur la théorie générale des surfaces et les applications géométriques du calcul infinitésimal: ptie. Déformation infiniment petite et répresentation sphérique. Notes et additions: I. Sur les méthodes d'approximations successives dans la théorie des équations différentielles, par E. Picard. II. Sur les géodésiques à intégrales quadratiques, par G. Koenigs. III. Sur la théorie des équations aux dérivées partielles du second ordre, par E. Cosserat. IV-XI. Par l'auteur. 1896.* Gauthier-Villars, 1896.

[93] George Dassios. On the capacity and rayleigh scattering for a class of non-convex bodies. *The Quarterly Journal of Mechanics and Applied Mathematics*, 42(3):467–475, 1989.

[94] Tadej Kotnik, Feda Bobanović, and Damijian Miklavčič. Sensitivity of transmembrane voltage induced by applied electric fields—a theoretical analysis. *Bioelectrochemistry and bioenergetics*, 43(2):285–291, 1997.

[95] Lianne A Cartee and R Plonsey. The transient subthreshold response of spherical and cylindrical cell models to extracellular stimulation. *IEEE transactions on biomedical engineering*, 39(1):76–85, 1992.

[96] Tadej Kotnik and Damijan Miklavčič. Second-order model of membrane electric field induced by alternating external electric fields. *IEEE Transactions on Biomedical Engineering*, 47(8):1074–1081, 2000.

[97] Katherine A DeBruin and Wanda Krassowska. Modeling electroporation in a single cell. i. effects of field strength and rest potential. *Biophysical journal*, 77(3):1213–1224, 1999.

[98] Gorazd Pucihar, Damijan Miklavcic, and Tadej Kotnik. A time-dependent numerical model of transmembrane voltage inducement and electroporation of irregularly shaped cells. *IEEE Transactions on Biomedical Engineering*, 56(5):1491–1501, 2009.

[99] David J Griffiths. *Introduction to electrodynamics.* Cambridge University Press, 2023.

[100] Ifunanya Nwogbaga and Brian A Camley. Coupling cell shape and velocity leads to oscillation and circling in keratocyte galvanotaxis. *Biophysical Journal*, 122(1):130–142, 2023.

[101] Leonard E Baum and Ted Petrie. Statistical inference for probabilistic functions of finite state markov chains. *The annals of mathematical statistics*, 37(6):1554–1563, 1966.

[102] Erich Leo Lehmann. *Elements of large-sample theory.* Springer, 1999.